TRANSPARENT PROCESS

OPEN ACCESS

THE EMBO JOURNAL

A kinesin-based approach for inducing chromosome-specific mis-segregation in human cells

My Anh Truong[1,2,†] (ID), Paula Cané-Gasull[1,2,†], Sippe G de Vries[1,2], Wilco Nijenhuis[3,4] (ID), René Wardenaar[5] (ID), Lukas C Kapitein[3,4], Floris Foijer[5] (ID) & Susanne MA Lens[1,2,*] (ID)

Abstract

Various cancer types exhibit characteristic and recurrent aneuploidy patterns. The origins of these cancer type-specific karyotypes are still unknown, partly because introducing or eliminating specific chromosomes in human cells still poses a challenge. Here, we describe a novel strategy to induce mis-segregation of specific chromosomes in different human cell types. We employed Tet repressor or nuclease-dead Cas9 to link a microtubule minus-end-directed kinesin (Kinesin14VIb) from *Physcomitrella patens* to integrated Tet operon repeats and chromosome-specific endogenous repeats, respectively. By live- and fixed-cell imaging, we observed poleward movement of the targeted loci during (pro)metaphase. Kinesin14VIb-mediated pulling forces on the targeted chromosome were counteracted by forces from kinetochore-attached microtubules. This tug-of-war resulted in chromosome-specific segregation errors during anaphase and revealed that spindle forces can heavily stretch chromosomal arms. By single-cell whole-genome sequencing, we established that kinesin-induced targeted mis-segregations predominantly result in chromosomal arm aneuploidies after a single cell division. Our kinesin-based strategy opens the possibility to investigate the immediate cellular responses to specific aneuploidies in different cell types; an important step toward understanding how tissue-specific aneuploidy patterns evolve.

Introduction

Aneuploidy, defined as a chromosome number that is not the exact multiple of the species haploid genome, is a prominent feature of cancer (Ben-David & Amon, 2020). Aneuploidy is the consequence of chromosomal instability (CIN), the increased frequency of chromosome segregation errors during mitosis that can result in gains or losses of entire chromosomes or of chromosomal arms in the daughter cells. Interestingly, different cancer types display different aneuploidy "signatures" with distinct whole-chromosome or arm-level gains and losses. For instance, colorectal cancers frequently display gains of chromosome 7, 13, and 20q, and a loss of chromosome 18, while low-grade gliomas are characterized by loss of 1p and gain of 19q (Duijf *et al*, 2013; Zack *et al*, 2013; Knouse *et al*, 2017; Sack *et al*, 2018; Taylor *et al*, 2018; Gerstung *et al*, 2020). How these tissue-specific aneuploidy patterns arise is currently unclear, but potential mechanisms include nonrandom chromosome mis-segregation and selective pressures on cells with gains and losses of particular chromosomes. The relative contribution of each potential mechanism might differ between different tissues (Ben-David & Amon, 2020). Interestingly, conditions resulting in nonrandom chromosome mis-segregations have been identified in human cells (Worrall *et al*, 2018; Tovini & McClelland, 2019; Dumont *et al*, 2020; Klaasen *et al*, 2022). In addition, selective pressures that shape and stabilize the aneuploidy landscape over time have been described in yeast (Dunham *et al*, 2002; Gresham *et al*, 2008; Rancati *et al*, 2008; Ravichandran *et al*, 2018), as well as in human cells (Sareen *et al*, 2009; Ly *et al*, 2011; Ippolito *et al*, 2021; Lukow *et al*, 2021; Su *et al*, 2021). However, how different cell types immediately respond and adapt to different chromosome gains and losses, and how specific aneuploidies drive or contribute to carcinogenesis, is still unknown. This is partly due to the technical challenge of introducing or eliminating distinct chromosomes (Ben-David & Amon, 2020).

Various approaches have been developed to model specific whole-chromosome and arm-level aneuploidies, including microcell-

1 Oncode Institute, Utrecht, The Netherlands
2 Center for Molecular Medicine, University Medical Center Utrecht, Utrecht, The Netherlands
3 Cell Biology, Neurobiology and Biophysics, Department of Biology, Faculty of Science, Utrecht University, Utrecht, The Netherlands
4 Centre for Living Technologies, Alliance TU/e, WUR, UU, UMC Utrecht, Utrecht, The Netherlands
5 European Research Institute for the Biology of Ageing (ERIBA), University of Groningen, University Medical Center Groningen, Groningen, The Netherlands
*Corresponding author. Tel: +31 88 7568114; E-mail: s.m.a.lens@umcutrecht.nl
†These authors contributed equally to this work

mediated chromosome transfer (Upender *et al*, 2004), Cre-lox recombination of homologs to generate acentric and dicentric chromosomes (Thomas *et al*, 2018), CRISPR/Cas9-mediated arm-level and whole-chromosome deletion (Adikusuma *et al*, 2017; Taylor *et al*, 2018), and centromere inactivation of chromosome Y by inducible degradation of CENP-A (Ly *et al*, 2016). Although these methods have generated valuable cell lines with particular chromosomal gains and losses (Nicholson *et al*, 2015; Passerini *et al*, 2016), all of these approaches rely on clonal expansion, and therefore cells may have evolved during cell culture following the initial karyotype change. Complementary to these targeted studies, others have assessed the short- and longer-term consequences of random karyotype changes in human cells predominantly after mitotic checkpoint inhibition (Santaguida *et al*, 2017; Soto *et al*, 2017; Viganó *et al*, 2018; Hintzen *et al*, 2022). Here, we introduce a novel approach to generate recent chromosome-specific aneuploidies in human cells, through targeted mis-segregation of specific chromosomes during mitosis. Leveraging the strong microtubule minus-end-directed transport capacity of the spreading earthmoss (*Physcomitrella patens*, *Pp*) Kinesin14VIb (Jonsson *et al*, 2015), we managed to manipulate the orientation of a chromosome of interest on the mitotic spindle. We tethered *Pp* Kinesin14VIb to an integrated TetO repeat, or to endogenous chromosome-specific repetitive loci using TetR or nuclease-dead Cas9 (dCas9), respectively. We show that the accumulation of this motor protein on either a subtelomeric repeat of chromosome 1p or a pericentromeric repeat of chromosome 9q counteracts the congressional forces acting on the targeted sister chromatids during early mitosis and caused their specific mis-segregation during anaphase. Finally, we demonstrate that this strategy gives rise to daughter cells with specific arm-level gain or loss of the targeted chromosome(s) after one cell division cycle.

Results

Tethering of Kin14VIb to a subtelomeric TetO locus in Chr1 leads to its unequal distribution during mitosis

A prerequisite for error-free chromosome segregation during mitosis is that all chromosomes align and biorient on the mitotic spindle. Biorientation and alignment are facilitated by the action of various plus-end-directed microtubule-based motors that guide the movement of chromosomes toward the spindle equator (Maiato *et al*, 2017). We hypothesized that by enriching minus-end-directed motors on a chromosome of interest, we could in turn transport that chromosome toward the spindle poles, causing it to misalign (Fig 1A, left). To test this hypothesis, we employed a minus-end-directed kinesin from *P. patens* (*Pp*), Kinesin14VIb, which has several attractive properties. First, *Pp* Kinesin14VIb is the fastest known minus-end-directed kinesin (Jonsson *et al*, 2015). Second, this plant motor shares very little homology with human kinesins (Shen *et al*, 2012; Nijenhuis *et al*, 2020); therefore, *Pp* Kinesin14VIb overexpression is unlikely to interfere with their function. Third, we recently demonstrated that a truncated version of *Pp* Kinesin14VIb (amino acids 861-1321), lacking its cargo binding domain, could efficiently induce retrograde transport of organelles in human interphase cells (Nijenhuis *et al*, 2020). This truncated variant of *Pp* Kinesin14VIb was used in this study and is referred to as Kin14VIb.

To establish whether Kin14VIb can promote minus-end-directed transport of a human mitotic chromosome, we made use of a U-2 OS cell line harboring a 200 × 96-mer TetO repeat in a subtelomeric region of one copy of Chr1p36 (Janicki *et al*, 2004; referred to as U-2 OS TetO, Fig 1A, right). To couple Kin14VIb to the chromosome with the TetO integration (referred to as the TetO chromosome), we fused the motor to the reverse Tet repressor and GFP (rTetR-GFP-Kin14VIb, Fig 1A, right). Expression of rTetR-GFP was used as control (ctrl), and binding of rTetR-GFP or rTetR-GFP-Kin14VIb to the TetO locus was induced by doxycycline addition. By live-cell imaging, we followed the trajectory of the TetO locus during mitosis (Fig 1B, Movies EV1–EV3 and Appendix Fig S1). Because binding of rTetR-fusion proteins to TetO repeats can interfere with replication of this repeat during S phase (Jacome & Fernandez-Capetillo, 2011; Beuzer *et al*, 2014), we added doxycycline immediately before filming to ensure that the captured mitotic cells were past S phase at the start of the experiment. In most control cells, the TetO focus aligned on the metaphase plate and was subsequently separated during anaphase (Fig 1B–D and Movie EV1). The two sister TetO foci segregated toward opposite spindle poles and eventually ended up in separate daughter nuclei (1-1 distribution, Fig 1B and D). In ~90% of rTetR-GFP-Kin14VIb-expressing cells, however, the TetO focus was found outside the metaphase plate (Fig 1B and C). During

Figure 1. Consequences of Kin14VIb enrichment on a subtelomeric TetO repeat in Chr1.

A   Left: Schematics of the rationale of our kinesin-based chromosome mis-segregation approach. Chromosome congression toward the spindle equator is facilitated by KT-MT attachments and plus-end-directed microtubule-based motors, such as chromokinesins at chromosome arms, and CENP-E at kinetochores (KTs). The minus-end-directed motor protein, Kin14VIb from *Physcomitrella patens* (orange), is expected to induce poleward transport and counteract the plus-end-directed motors. Right: In the U-2 OS TetO cells, a 200 × 96mer TetO repeat is integrated in a subtelomeric region of the p arm of one of the chromosomes 1 (Janicki *et al*, 2004). Kin14VIb is fused to GFP and rTetR, allowing doxycycline-inducible binding to the TetO repeat.

B–E   Live-cell microscopy of U-2 OS TetO cells expressing rTetR-GFP (ctrl), or rTetR-GFP-Kin14VIb (Kin14VIb; Movies EV1–EV3). (B) Representative stills showing the most frequently observed metaphase localization and daughter nuclei distribution of the duplicated TetO locus (white arrowheads). Chromatin was visualized through expression of H2B-mCherry; GFP depicts the TetO locus. Due to the presence of a predicted NES sequence in Kin14VIb, the TetO locus only becomes visible at NEB in Kin14VIb-expressing cells. Time = h:min, scale bar = 5 μm. Schemes illustrating the metaphase localization of the TetO locus and its subsequent distribution over daughter nuclei are shown on the right. (C) Quantification of the metaphase localization of the TetO locus. Out = TetO locus observed outside the metaphase plate. (D) Quantification of the distribution of the duplicated TetO locus over the main daughter nuclei after anaphase. See Fig EV3B and Appendix Fig S1, for example, of 1-0 and 1-1split, respectively. (E) Time between nuclear envelope breakdown (NEB) and anaphase onset of the indicated cell categories. Each dot represents an individual cell.

Data information: N = 59 cells for ctrl, n = 57 cells for Kin14VIb. All analyses come from one single experiment. In (E), mean ± S.D. is shown. Ns = not significant, ***P < 0.001 (Kruskal–Wallis and a Dann's multiple comparison test).
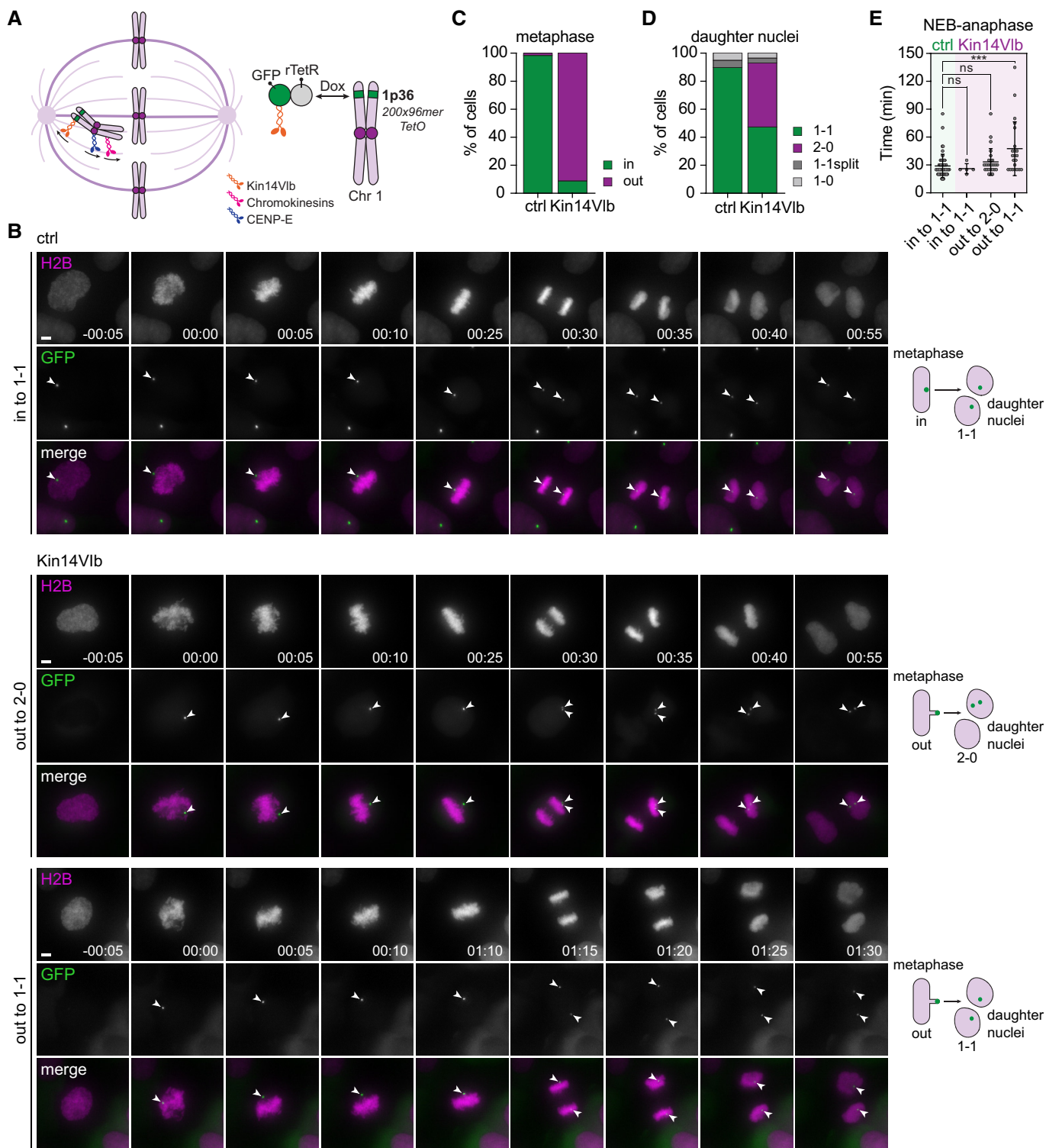
Figure 1.

the subsequent anaphase, the sister TetO foci co-segregated into one of the daughter nuclei, resulting in a 2-0 distribution of the TetO locus in ~45% of cell divisions (Fig 1B and D and Movie EV2). In addition, in ~40% of dividing cells expressing rTetR-GFP-Kin14VIb, we observed that the TetO locus initially localized outside the metaphase plate, but eventually segregated equally into the two daughter nuclei in the subsequent anaphase (1-1 distribution, Fig 1B–D and Movie EV3). Of note, in rTetR-GFP-Kin14VIb-expressing cells, a 1-1 distribution of the TetO locus appeared variable and was in some experiments hardly observed (Fig EV1A). This

is most likely explained by experimental and cell-to-cell variation of rTetR-GFP-Kin14VIb expression levels, as we measured on average higher GFP fluorescence intensity levels in the group of cells displaying a 2-0 distribution of the TetO locus compared to cells displaying a 1-1 distribution of the locus (Fig EV1B). Collectively, our live-cell imaging data suggest that rTetR-GFP-Kin14VIb can misalign a duplicated TetO locus during mitosis and cause its subsequent unequal distribution across daughter nuclei.

Kin14VIb-enrichment near telomeres does not prevent kinetochore–microtubule attachment

We observed a ∼ 30-min delay in anaphase onset in cells where the TetO locus initially resided outside the metaphase plate, but was segregated equally during anaphase (Fig 1E, category "out to 1-1"). However, the unequal (2-0) distribution of the duplicated TetO locus in Kin14VIb-expressing cells was not accompanied by a

delay in anaphase onset (Fig 1E). This suggested that the kinetochores (KTs) of the Kin14VIb-bound TetO chromosome had acquired microtubule (MT) attachments that silenced the mitotic checkpoint (Etemad *et al*, 2015; Kuhn & Dumont, 2017). To substantiate this, we performed immunofluorescence (IF) to assess TetO chromosome positioning and KT orientation in fixed U-2 OS cells synchronized in metaphase using the proteasome inhibitor MG132. Consistent with the live-cell imaging data (Fig 1B and C), we detected the TetO locus inside the metaphase plate in nearly all control cells but not in Kin14VIb expressing cells (Fig 2A and C). In 53–71% of Kin14VIb-expressing cells, the TetO locus was found near one of the spindle poles, causing the p arms of the TetO sister chromatids to stick out from the metaphase plate ("arms out," Fig 2A–D). Occasionally, we observed the TetO locus to be stretched between the spindle pole and metaphase plate, or to be disconnected from the chromosome ("stretched/fragmented," Fig 2B and D). Typically, we did not detect the centromere protein
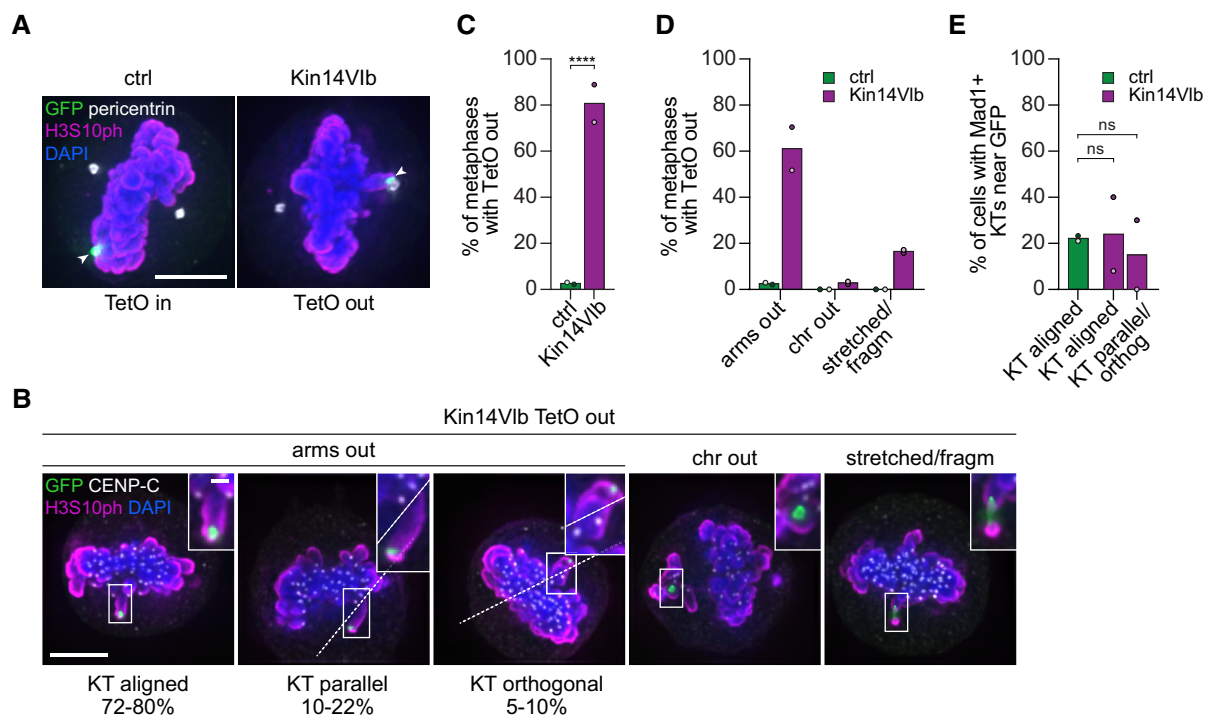

Figure 2. Metaphase orientation and KT attachment status of the Kin14VIb-bound TetO chromosome.

A   IF for pericentrin, GFP, H3S10ph of U-2 OS TetO cells in metaphase. The TetO locus (GFP focus, white arrowhead) is aligned on the metaphase plate (TetO in) in cells expressing rTetR-GFP (ctrl) or co-localizes with one of the two pericentrin-marked centrosomes (TetO out) in rTetR-GFP-Kin14VIb-expressing cells (Kin14VIb). Scale bar = 5 μm. For clarity, the maximum intensity projection of a subset of z stacks (25–30/50) is shown.

B–D IF for CENP-C, GFP, H3S10ph of U-2 OS TetO cells in metaphase and expressing rTetR-GFP-Kin14VIb. (B) Representative images of the different orientations of the TetO chromosome and sister KTs (scale bar = 5 μm). Magnifications of the white boxed regions containing the TetO chromosome are shown in the corners of the images (scale bar = 1 μm). For clarity, the maximum intensity projection of a subset of z stacks (6–7/50) is shown for each image. Numbers below the images depict the frequency of the indicated orientation of the sister KTs of the duplicated TetO chromosome with its p arm sticking out toward the spindle pole (arms out). KTs aligned: sister KTs buried inside the metaphase plate; KTs parallel: intersister KT axis (dotted line) is (near-)parallel the metaphase plate; KTs orthogonal: intersister KT axis perpendicular to metaphase plate. (C) Quantification of the fraction of ctrl or Kin14VIb-expressing cells with the TetO locus observed outside the metaphase plate (TetO out). (D) Deconstruction of (C). Fraction of cells with the indicated orientation of the duplicated TetO locus and TetO chromosome.

E   Quantification of the number of cells with Mad1-positive KTs nearby the TetO locus. Representative IF images are shown in Appendix Fig S2. In case the KTs of the TetO chromosome were aligned, we scored whether KTs in the vicinity of the TetO locus were Mad1^{+}. In case the KTs of the TetO chromosome could be distinguished in rTetR-GFP-Kin14VIb-expressing cells (with either orthogonal or parallel oriented KTs), we scored if at least one of the KTs was Mad1^{+}.

Data information: Bars represent the mean of 2 biological replicates, while dark- and light-colored dots represent the values of each experiment. (C, D): N ≥ 29 cells per condition, per experiment, ****P < 0.0001; Fisher's exact test. (E): N ≥ 27 cells per condition, per experiment, (ns) not significant; Fisher's exact test.

CENP-C in the vicinity of the TetO locus at the spindle poles. Instead, in 72–80% of the cells displaying the TetO locus outside the metaphase plate, the KTs of the Kin14VIb-bound chromosomes were buried inside the metaphase plate together with the other aligned KTs (Fig 2B). In a few cases, we could distinguish the KTs of the TetO chromosome from the other KTs, with the intersister KT axis either orthogonal or near-parallel to the metaphase plate (Fig 2B). We then performed IF for the mitotic checkpoint protein Mad1, using its absence from KTs as a marker for MT attachment (Musacchio & Salmon, 2007). When assessing the Mad1 status of KTs nearby the TetO locus, we did not find a consistent difference between control cells (with TetO locus inside the metaphase plate) and Kin14VIb-expressing cells (with TetO locus outside the metaphase plate; Fig 2E and Appendix Fig S2). Moreover, in the few cells in which we could distinguish the KTs of the TetO chromosome, the sister KTs of this chromosome were predominantly attached (i.e., Mad1 negative), irrespective of whether the intersister KT axis was orthogonal or near-parallel to the metaphase plate (Fig 2E and Appendix Fig S2). Thus, recruiting minus-end-directed kinesins near chromosomal telomeres allowed the KTs of that chromosome to attach to microtubules.

Kin14VIb binding causes on-target mis-segregation of the TetO chromosome during anaphase

To understand how simultaneous pulling by KT-attached MTs and Kin14VIb would affect chromosome orientation and segregation during anaphase, we analyzed fixed anaphases of control and Kin14VIb-expressing cells with a 1-1, or a 2-0 distribution of the TetO locus (Figs 3A and B, and EV1A). We observed that $38 \pm 18\%$ of rTetR-GFP expressing cells displayed chromosome bridges or lagging chromosomes that did not involve the TetO chromosome, illustrating the rate of ongoing CIN in U-2 OS cells, as reported previously (Bakhoum et al, 2009; Fig 3A and B). Interestingly, bridging or lagging chromatin was observed in 100% of the Kin14VIb-expressing cells displaying a 2-0 distribution of the TetO locus (Fig 3A and B), indicating that tethering of the kinesin to the TetO chromosome significantly increased CIN. Interestingly, in contrast to both ctrl or Kin14VIb-expressing cells displaying a 1-1 distribution, in cells with a 2-0 distribution of the TetO locus, we frequently ($92 \pm 3\%$) detected at least one stretch of chromatin that was in line with the GFP$^+$ TetO locus (Fig 3A, dark and light purple bars, and Fig EV1C). Within this fraction, we recurrently ($78 \pm 16\%$) observed a stretched chromatid arm, with the TetO locus residing near one of the spindle poles and its KT lagging behind the two main masses of segregating chromosomes (Fig 3A, B, and E). Occasionally, we found the arms of both sister chromatids being stretched in Kin14VIb-expressing cells, most likely reflecting syntelic attachment of the sister KTs by MTs coming from the spindle pole, opposite from the one to which the TetO locus is transported (Figs 3A and EV1D; Godek et al, 2015). Thus, Kin14VIb-mediated poleward transport of the subtelomeric TetO locus induces a specific type of segregation error in anaphase: a heavily stretched p arm of a single sister chromatid. Our data suggest that while each p arm of the duplicated TetO chromosome is pulled toward one spindle pole by Kin14VIb, one KT of this duplicated chromosome is attached to MTs coming from the opposite spindle pole (Fig 3A, B, and E).

Tethering of Kin14VIb to a subtelomeric TetO repeat in Chr1 results in 1p copy number alterations after a single cell division

Depending on the counteracting forces exerted by the KT-attached MTs and the TetO-bound Kin14VIb, we anticipated that the stretched sister chromatid would either be mis-segregated toward the TetO locus, or be further stretched by spindle forces, with the KT moving toward one spindle pole and the TetO locus toward the opposite spindle pole, causing the p arm to cross and persist in the cytokinetic furrow. Analysis of late anaphases and telophases with a 1-1 and 2-0 distribution of the TetO locus revealed that the 2-0 distribution was frequently ($77 \pm 8\%$) accompanied by a chromatin bridge inside the furrow, or by a spike of chromatin with strong phosphorylation of histone H3 Serine10 (H3S10ph) in at least one of the future daughter nuclei (Figs 3C and D, and EV1E). H3S10 is a substrate of the Aurora B kinase, and phosphorylation of this histone site during anaphase and telophase suggests close proximity to, or recent passing through the spindle midzone and midbody, structures on which Aurora B localizes during this phase of the cell cycle (Fuller et al, 2008; Maiato et al, 2015; Fig EV1E). We subsequently assessed how frequently the Chr1 centromere would be unequally distributed over the future daughter nuclei of Kin14VIb-expressing cells, by labeling Chr1 centromeres using FISH (chr1-CEN). Note that U-2 OS is predominantly triploid for Chr1 (Figs 4A and EV2B) and that we could not select for cells expressing rTetR-GFP-Kin14VIb nor with a 2-0 TetO locus distribution since we were unable to reliably combine IF with FISH. We observed deviations in the segregation of Chr1 centromeres in 29–38% of the Kin14VIb transduced anaphase cells, compared with 8–10% in control cells (Fig 4A and B). In agreement with the IF data (Fig 3), we more frequently detected chr1-CEN foci lagging behind the main masses of segregating chromosomes in Kin14VIb expressing cells ('lagging'), as well as chr1-CEN foci that we considered late arrivals in the correct future daughter nucleus due to Kin14VIb-dependent transport of the chromosomal arm toward the opposite spindle pole ("late-equal"). The latter foci typically resided near the edge of one of the segregated chromosome masses and were connected to a chromatin bridge. In both ctrl and Kin14VIb-expressing cells, we occasionally detected fragmented chr1-CEN FISH signals in a chromatin bridge ("bridging"). Only 9–11% of the Kin14VIb-expressing cells displayed an unequal distribution of chr1-CEN across future daughter nuclei versus 2–4% in ctrl. Because the lagging centromeres might eventually be segregated into the "correct" daughter nucleus (Sen et al, 2021), we only considered the unequally distributed chr1-CEN foci as a potential proxy for a whole Chr1 mis-segregation (Fig 4A and B). Based on the combined IF and centromere FISH data (Figs 3A–D and 4A and B), we estimate that Kin14VIb binding close to the telomere may only cause a whole Chr1 mis-segregation and subsequent aneuploidy in a very small fraction (< 10%) of dividing cells, but most likely causes Chr1p copy number alterations after most cell divisions. Accordingly, shallow whole-genome sequencing (WGS) of single G1 nuclei (scKaryo-Seq) of U-2 OS TetO cells (Fig EV2A–C) revealed an increased mis-segregation rate for Chr1p specifically in rTetR-GFP-Kin14VIb transduced cells, evidenced by an increased aneuploidy score for this chromosome arm (Fig 4C and Table EV1). Note that all chromosome arms displayed variations due to the overall heterogeneous nature of U-2 OS karyotypes, but that 1p exhibited the highest increase in aneuploidy score among all chromosome arms when rTetR-GFP-Kin14VIb
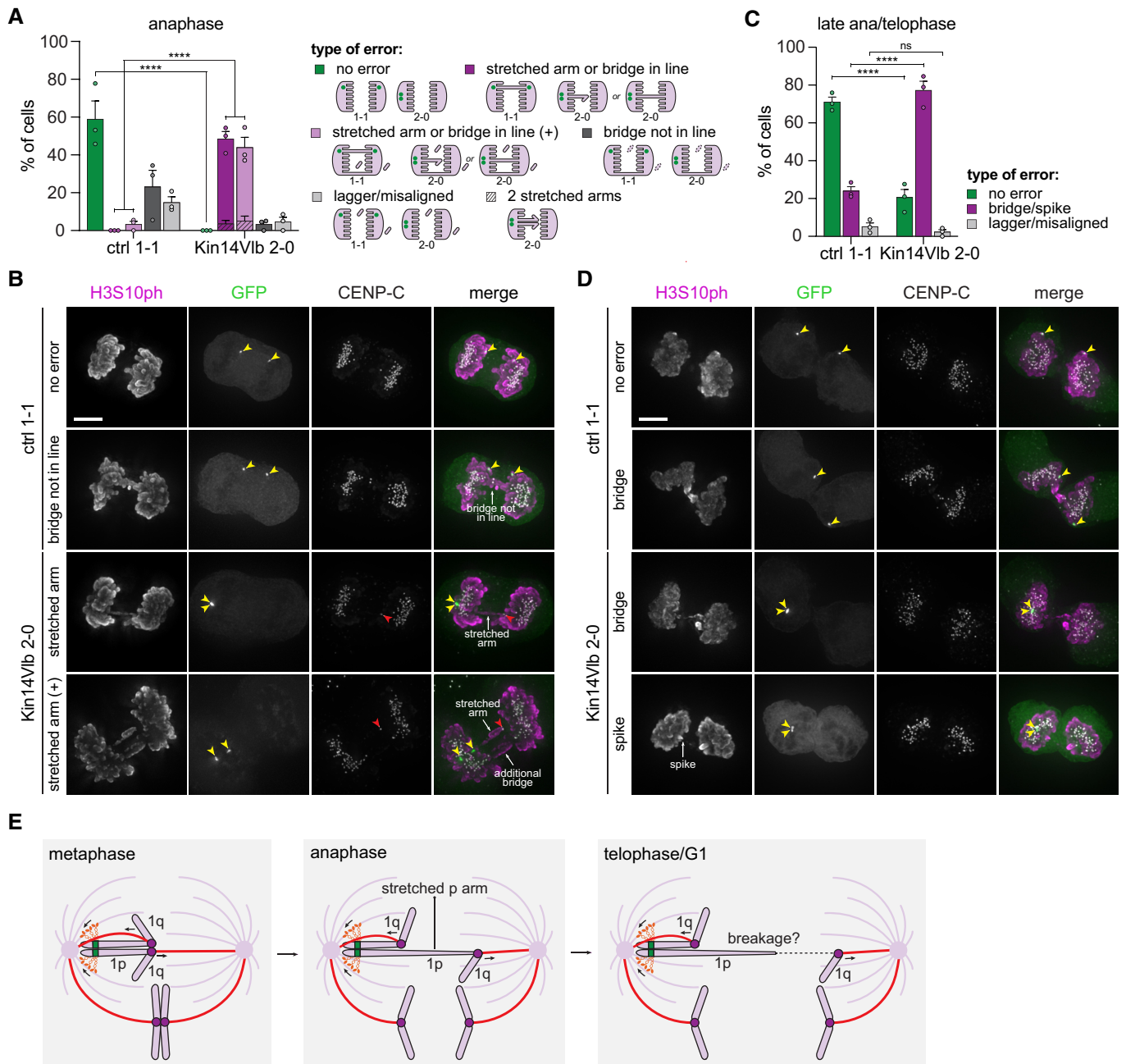
Figure 3. Opposing pulling forces acting on the Kin14IVb-bound TetO chromosome causes its stretching and unequal segregation during anaphase.

A–D (A, C) Frequencies of the different types of segregation errors observed during anaphase (A) and late anaphase/telophase (C). Schemes illustrating the observed types of anaphase errors are shown on the right of (A). Cells within the main TetO locus distribution categories in control (1-1), and Kin14VIb (2-0) conditions were scored (see also Fig EV1A). The majority of Kin14VIb-expressing anaphases display at least one stretched arm (CENP-C in line with TetO locus at the pole) or a bridge in line with the TetO locus at the pole ("stretched arm or bridge in line"), some of them with additional bridges (+). (B, D) IF images for CENP-C, GFP, H3S10ph of U-2 OS TetO cells in anaphase (B) and late anaphase or telophase (D), expressing either rTetR-GFP or rTetR-GFP-Kin14VIb. Images (maximum intensity projections) represent the most frequently observed anaphase and telophase errors in cells with either a 1-1 (majority of events in ctrl), or 2-0 (majority of events in Kin14VIb) TetO locus distribution. Scale bar = 5 μm. Yellow arrowheads indicate TetO locus and red arrowheads CENP-C.

E Schemes illustrating the orientation and mis-segregation of the duplicated TetO chromosome in metaphase, anaphase, and telophase induced by rTetR-GFP-Kin14VIb binding to the TetO locus.

Data information: (A, C): Means ± S.E.M. of 3 biological replicates are shown. Dots represent the values of each experiment. N = 41–89 cells per condition, per experiment (see also Fig EV1A for numbers). ****P < 0.0001, (ns) not significant; Fisher's exact test. (B, D): for optimal visibility of the TetO foci, the brightness and contrast of all channels were linearly adjusted for individual cells.
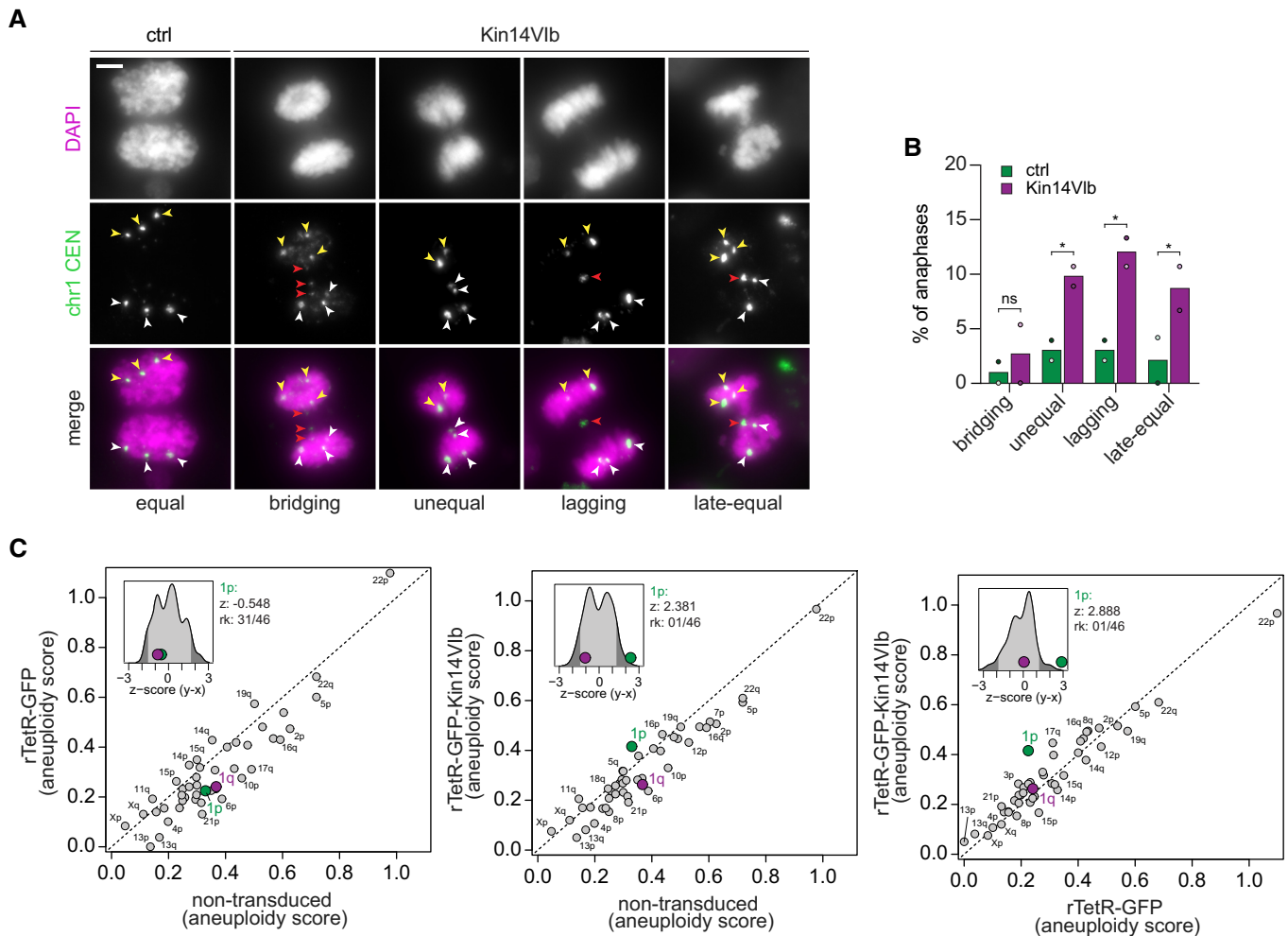
Figure 4. Tethering of Kin14VIb to a subtelomeric TetO repeat in Chr1p leads to 1p copy number alterations after a single cell division.

A   Representative images of U-2 OS TetO anaphases/telophases expressing rTetR-GFP or rTetR-GFP-Kin14VIb with FISH-marked centromeres of chromosome 1 (chr1-CEN). White and yellow arrowheads: chr1-CEN segregated into the main masses of segregating chromosomes; red arrowheads: chr1-CEN FISH signal fragmented or splitted in a bridge (bridging); chr1-CEN lagging between the two main masses of segregating chromosomes (lagging); chr1-CEN late arrival (late-equal: one CEN focus in but near the edge of a separated chromosome mass and connected to a bridge). For clarity, the maximum intensity projection of a subset of z stacks (6–12/64) is shown. Scale bar = 5 μm.
B   Frequency of the different types of errors observed in A. The mean (bars) and individual values (dots) of 2 independent experiments are shown.
C   Plots comparing aneuploidy scores of all chromosomal p and q arms between nontransduced U-2 OS TetO cells and rTetR-GFP-transduced cells (left), nontransduced cells and rTetR-GFP-Kin14VIb-transduced cells (middle), and rTetR-GFP-transduced and rTetR-GFP-Kin14VIb-transduced cells (right). Aneuploidy scores were calculated from the scKaryo-Seq data of single G1 nuclei following a round of mitosis with doxycycline-induced rTetR-TetO binding. The median copy number of each bin (median across libraries) was determined for the nontransduced U-2 OS TetO condition and used as reference (see Fig EV2B). The aneuploidy scores of the chromosomal arms are deviations from this reference (average absolute difference of the bins that are associated with the arm). Inserts show density plots of the difference of the scores of the two conditions that are compared (y-axis minus x-axis). Differences are expressed as z-scores (number of standard deviations from the mean). The 95% confidence interval is depicted in light gray. The values of the 1p and 1q arm are indicated with a green and purple dot, respectively. Z-score value for 1p and its ranking (rk) is indicated (see Table EV1).

Data information: In (A), for optimal visibility of the chr1-CEN FISH foci, the brightness and contrast were linearly adjusted for individual cells. (B): n ≥ 45 cells per condition, per experiment. Bars represent the mean of 2 biological replicates, while dark- and light-colored dots represent the values of each experiment. *P < 0.05, (ns) not significant. Fisher's exact test.

was transduced (Fig 4C and Table EV1). Although the IF, Chr1-CEN FISH, and scKaryo-Seq data suggest that the Chr1p arm breaks during cell division, we did not detect an increase in the double-strand break (DSB) marker γH2AX on the TetO locus, nor on the H3S10ph+ chromatin bridges in Kin14VIb-expressing telophase cells (Appendix Fig S3A–C; Sedelnikova et al, 2002). This suggests that persistent

stretching of the p arm per se does not cause detectable DNA damage during late anaphase/telophase and that the actual breakage occurs later (e.g., during abscission; Maciejowski et al, 2015; Umbreit et al, 2020) or that the DNA damage is detected later (e.g., in G1; Janssen et al, 2011). Because chromosome bridge resolution is often accompanied by micronuclei (MN) formation in G1 (Maciejowski

et al, 2015; Umbreit *et al*, 2020; Krupina *et al*, 2021), we analyzed later time points of the live-cell imaging experiment for the appearance of MN (Figs 1B and EV3A and B). For ∼ 21% of the cell divisions with a 2-0 distribution of the TetO locus, we detected a GFP-negative MN in at least one of the two daughter cells, compared with 4–9% of the divisions with 1-1 distribution of the locus (Fig EV3A). The observation that these MN were GFP-negative implied that resolution of the stretched Chr1p arm did not involve the subtelomeric TetO locus. Collectively, our data suggest that Kin14VIb-mediated poleward transport of a subtelomeric repeat in Chr1p causes stretching of a single chromatid arm and subsequent breakage of this arm after mitosis, leading to copy number alterations of Chr1p in the resulting daughter cells.

Harnessing dCas9 to link Kin14VIb to endogenous chromosome-specific DNA repeats in RPE1 cells

Having established a tool to robustly induce the mis-segregation of specific single chromatid arms, we aimed at making this technology more broadly applicable. To facilitate its introduction into more physiological model systems, we removed the dependence on chromosomal integration of exogenous repetitive DNA sequences by employing nuclease-dead Cas9 (dCas9) to link Kin14VIb to chromosome-specific endogenous repeats (Gilbert *et al*, 2013). To tether Kin14VIb to dCas9 on a targeted endogenous locus, we made use of FK506 binding protein 12 (FKBP12) and the FKBP-rapamycin binding (FRB) domain, which can be chemically induced to heterodimerize upon the addition of rapalog (Rivera *et al*, 1996; Liberles *et al*, 1997; Fig 5A). Additionally, to increase Kin14VIb-mediated pulling efficiency, we attached the dimerization domain GCN4 to mCherry-tagged FRB-Kin14VIb, thereby clustering Kin14VIb into dimer of dimers and rendering the motor highly processive, independently of cargo binding (Jonsson *et al*, 2015; Nijenhuis *et al*, 2020; Fig 5A and Appendix Fig S4A–C). We generated a nontransformed, near-diploid human retinal pigment epithelial (RPE1) cell line stably expressing dCas9-GFP-3xFKBP, allowing us to both target and visualize specific loci using live-cell imaging. This cell line also expressed FRB-mCherry-GCN4-Kin14VIb under the control of a doxycycline-inducible promotor (Appendix Fig S4D). From this FACS-sorted polyclonal cell line, monoclonal cell lines were derived and screened for efficient Kin14VIb-mediated poleward transport using a simple high-throughput assay: cells treated with the Eg5 inhibitor STLC were scored for their capacity to recruit the dCas9-GFP-3xFKBP-bound loci toward the centrosomes of a monopolar spindle after rapalog addition (Appendix Fig S4A and C). The monoclonal cell line that performed best in this assay was selected for further studies and is referred to as RPE1 dCas9-Kin14VIb (Appendix Fig S4C–F). In agreement with earlier observations (Nijenhuis *et al*, 2020), GCN4-Kin14VIb weakly decorated the spindle poles, occasionally resulting in dCas9-GFP-3xFKBP localization at these sites (Movies EV4–EV8).

We then tested whether directing Kin14VIb to an endogenous subtelomeric repeat would have similar consequences for the targeted chromosome as Kin14VIb binding to a large integrated subtelomeric TetO repeat. To this end, we transduced RPE1 dCas9-Kin14VIb cells with a sgRNA targeting dCas9 to a DNA repeat in Chr1p36 (Chr1-telo, Fig 5B; Ma *et al*, 2016; Dumont

et al, 2020). After rapalog addition, metaphase-arrested RPE1 cells displayed the typical phenotype of chromosomal arms sticking out from the metaphase plate, with the dCas9-bound subtelomeric locus facing the spindle pole (Fig 5C), similar to U-2 OS TetO cells expressing Kin14VIb (Fig 2A). We next followed the alignment and segregation of the two Chr1-telo loci over time by tracking the GFP foci throughout mitosis by live-cell imaging immediately after the addition of rapalog (Fig 5D). While most control cells showed complete alignment of both Chr1-telo loci in metaphase, rapalog-treated cells frequently displayed at least one Chr1-telo locus outside the metaphase plate (Fig 5D and E). Similar to observations in fixed cells (Fig 5C), three distinct categories of foci residing "outside" the metaphase plate could be distinguished: (i) one of the foci aligned while the other was located near a spindle pole, (ii) both foci resided near the same pole, or (iii) the two foci were found near opposite spindle poles (Fig 5C–E). In the subsequent anaphase, these orientations mostly led to a Chr1-telo locus distribution between daughter nuclei of, respectively, 3-1, 4-0, or 2-2 with sister loci ending up in the same daughter nuclei (2-2, same sisters; Fig 5D and E). Although Chr1p pulling and mis-segregation efficiency varied per experiment and was lower than observed for the U-2 OS TetO cells (Appendix Fig S4B and C), an unequal distribution of the Chr1-telo loci was consistently observed in the rapalog-treated RPE1 cells (Fig 5E).

Inducing targeted CIN of Chr9q in RPE1 cells

The versatile nature of the dCas9-based system in RPE1 cells allows targeting of Kin14VIb to other chromosomes and to other chromosomal regions. Therefore, we next studied the consequences of Kin14VIb binding to a chromosomal region more proximal to the kinetochore, by transducing a sgRNA specific to a pericentromeric DNA repeat of Chr9q12 (Chr9-cen, Fig 6A; Ma *et al*, 2015; Ma *et al*, 2018). Since this repeat is predicted to harbor ∼ 550,000 Chr9-cen sgRNA binding sites, while the subtelomeric repeat in Chr1p is predicted to harbor ∼ 1,400 Chr1-telo sgRNA binding sites (Tovini *et al*, 2023, accompanying article), Chr9-cen GFP foci appear larger than Chr1-telo GFP foci (Figs 5B and 6A and Appendix Fig S4G). Moreover, after rapalog addition, Chr9-cen GFP foci localized near the centrosomes of monopolar spindles more often than Chr1-telo GFP foci (Appendix Fig S4H). Live-cell microscopy showed that both Chr9-cen homologs were most frequently transported toward either the same (sp) or opposite (op) spindle pole (Fig 6B and C). Consequently, this recurrently led to daughter cells with a 4-0 or a 2-2 (same sisters) distribution of Chr9-cen foci (Fig 6B and C and Movies EV4, EV7 and EV8). Note that in the absence of rapalog, ∼ 30% of the cells already displayed some Chr9-cen specific anaphase errors (i.e., GFP-positive chromatin bridges or a lagging GFP[+] focus, Figs 6B and C, and 7C–F and Movies EV5 and EV6), sometimes leading to 3-1 focus distribution in the daughter cells (Fig 6C and Movie EV5). This might be a consequence of incomplete replication of the repeat caused by binding of dCas9 to the pericentromeric repeats on Chr9 during S phase (Whinn *et al*, 2019; Doi *et al*, 2021). Importantly, despite this higher background anaphase error rate, coupling Kin14VIb to Chr9-cen repeats, induced an increase in the unequal distribution of the Chr9-cen locus during mitosis (Fig 6C). Since Kin14VIb harbors a predicted nuclear export signal (NES), it is predominantly cytosolic during interphase, also
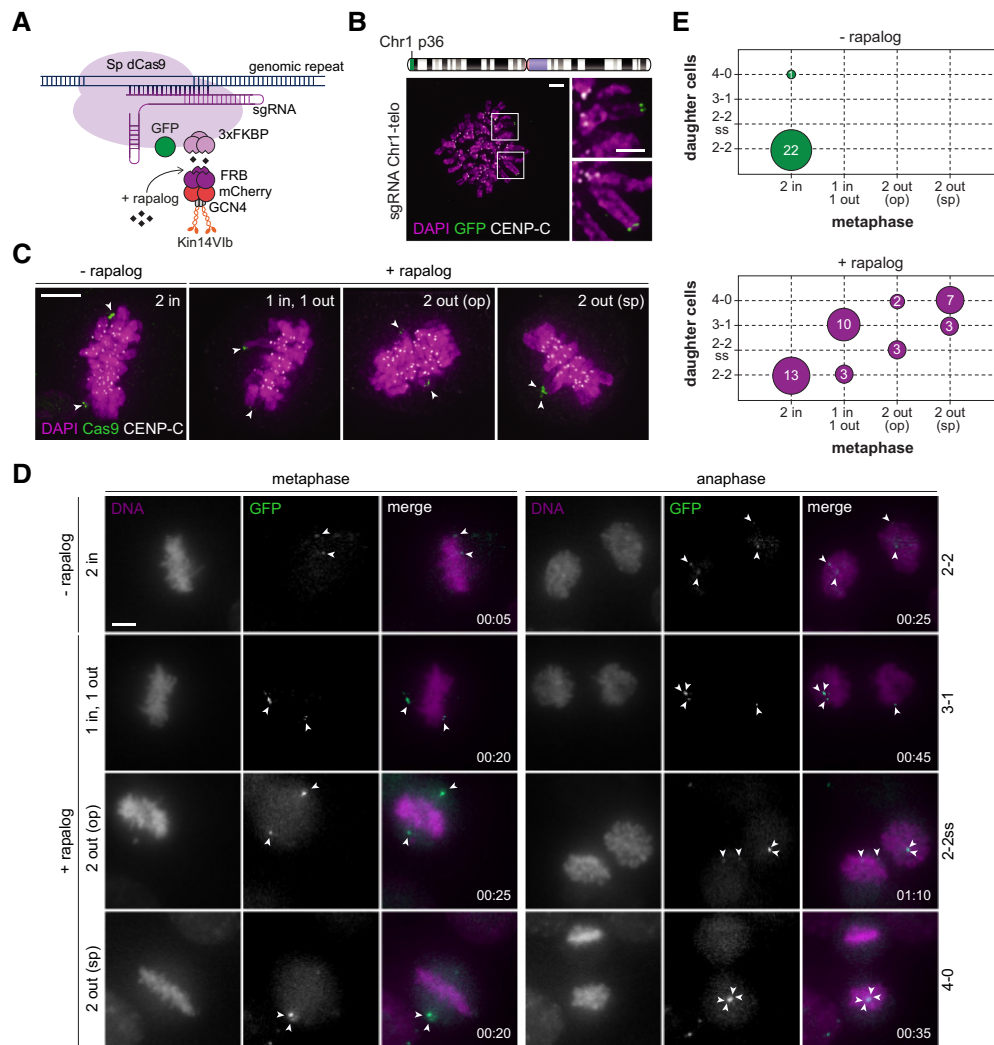
Figure 5. Tethering Kin14VIb to endogenous subtelomeric DNA repeats of Chr1p in RPE1 cells.

A   Schematic representation of our strategy to couple FRB-mCherry-GCN4-Kin14VIb to endogenous chromosome-specific loci in a dCas9-GFP-3xFKBP expressing RPE1 cell line.

B   The Chr1-telo sgRNA binds to a subtelomeric repetitive DNA sequence in the p arm of chromosome 1 (top). IF for CENP-C and GFP on chromosome spreads of RPE1 cells expressing dCas9-GFP-3xFKBP and transduced with Chr1-telo sgRNAs (bottom). Magnifications of the white boxed regions (each region showing one Chr1 homolog) are shown on the right of the IF image. Scale bars = 2 μm.

C   IF for Cas9 and CENP-C of metaphases of RPE1-dCas9-Kin14VIb cells transduced with Chr1-telo sgRNA in the presence or absence of 500 nM rapalog. The Chr1-telo loci (Cas9 foci, white arrowheads) are aligned on the metaphase plate in control condition (− rapalog), while the loci are facing either a single or opposite poles after rapalog addition to induce Kin14VIb binding to dCas9. Scale bar = 5 μm. For clarity, the maximum intensity projection of a subset of z stacks (18–50/100) is shown.

D, E   Live-cell microscopy of asynchronously growing RPE1-dCas9-Kin14VIb cells transduced with Chr1-telo sgRNA in the presence or absence of 500 nM rapalog to induce kinesin binding to the subtelomeric locus. (D) Stills showing the most frequently observed metaphase localization and daughter cell distribution (white arrowheads) of the duplicated Chr1-telo loci. SiR-DNA was used to visualize the DNA, GFP depicts the Chr1-telo loci. Time (h:min). Scale bar = 5 μm. Note that in the upper panel, the cell was already in mitosis when imaging started (*t* = 0:00). (E) Plots showing the relationship between the indicated metaphase orientation of the Chr1-telo loci, and the indicated distributions of the loci in the daughter cells. Circle size reflects relative cell numbers. The actual cell numbers per condition are indicated in the circles.

Data information: (D, E): Cells were derived from three independent imaging experiments. *N* = 23 cells (− rapalog), *n* = 41 cells (+ rapalog). Sp = same pole, op = opposite pole, ss = same sisters. (C, D): for optimal visibility of the Chr1-telo foci, the brightness and contrast of all channels were linearly adjusted for individual cells.

after rapalog addition (Appendix Fig S4E). FRB-mCherry-Kin14VIb is thus expected to predominantly bind to Chr9-cen after NEB, similar to rTetR-GFP-Kin14VIb in the U-2 OS TetO cells (Fig 1B, bottom panel). Hence, the increased unequal distribution of Chr9-cen in

rapalog-treated cells is unlikely to be caused by elevated replication defects induced by bulkier dCas9–Kin14VIb complexes binding to the repeat during S phase, but induced by Kin14VIb-dependent transport of Chr9 toward the spindle pole during mitosis.
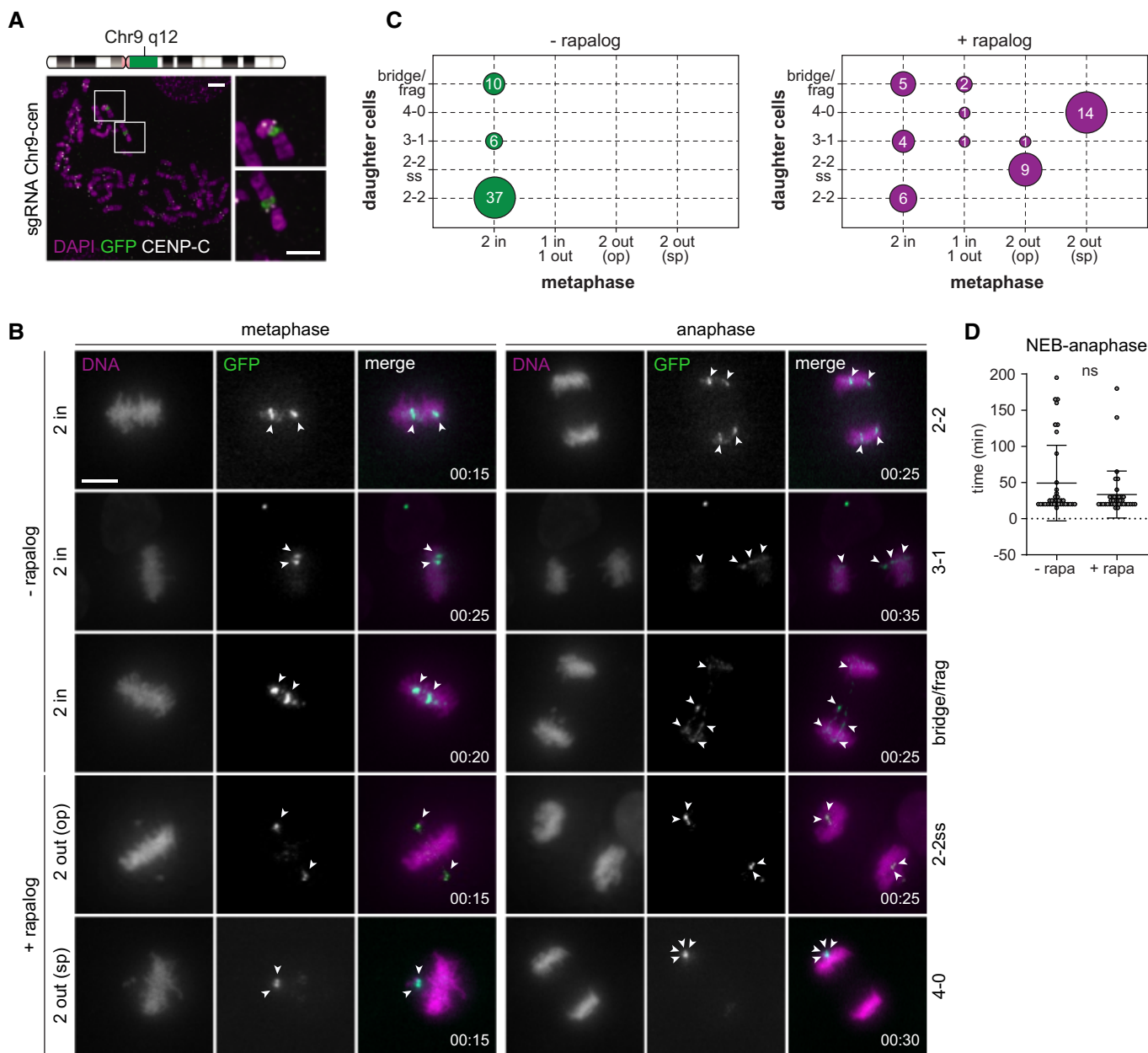
Figure 6. Coupling Kin14IVb to endogenous pericentromeric repeats of Chr9q in RPE1 cells.

A The Chr9-cen sgRNA binds to a pericentromeric repetitive DNA sequence in the q arm of chromosome 9 (top). IF of CENP-C and GFP on chromosome spreads of RPE1 cells expressing dCas9-GFP-3xFKBP and transduced with Chr9-cen sgRNAs (bottom). Magnifications of the white boxed regions (each region showing one Chr9 homolog) are shown on the right of the IF image (scale bars = 2 μm).

B, C Live-cell microscopy of asynchronously growing RPE1-dCas9-Kin14VIb cells transduced with Chr9-cen sgRNA and plus/minus rapalog to induce kinesin binding to the pericentromeric locus (Movies EV4–EV8). (B) Stills of the most frequently observed metaphase orientations and daughter cell distributions of the duplicated Chr9-cen loci (white arrowheads) are shown. SiR-DNA was used to visualize the DNA; GFP depicts the Chr9-cen loci. Time (h:min). Scale bar = 5 μm. (C) Plots showing the relationship between the indicated metaphase orientation of the Chr9-cen loci, and the indicated distributions of the loci over the daughter cells. Circle size reflects relative cell numbers. The actual cell numbers per condition are indicated in the circles.

D Time between nuclear envelope breakdown (NEB) and anaphase onset in the presence (Kin14VIb bound to dCas9) or absence (Kin14VIb expressed, but not bound to dCas9) of rapalog.

Data information: (B- D): Cells were derived from two independent imaging experiments. (C): N = 53 cells (− rapalog), n = 43 cells (+ rapalog). Sp = same pole, op = opposite pole, ss = same sisters. In (B), for optimal visibility of the Chr9-cen foci, the brightness and contrast of all channels were linearly adjusted for individual cells. See Movies EV4–EV8 for equally adjusted corresponding examples. (D): Mean and S.D. are shown. Dots represent individual cells from two independent imaging experiments. (Ns) not significant; Mann–Whitney test (n = 38 cells for both conditions as NEB-anaphase time was not quantified for cells in (C) that were already in mitosis at the start of the imaging experiment).

Kin14VIb binding to a pericentromeric DNA repeat in Chr9 separates 9q from 9p during mitosis

Detailed IF analysis of fixed mitoses revealed notable differences in the consequences of Kin14VIb binding near telomeres (Figs 2A–D and 5C) versus near centromeres (Fig 7A). In Chr9-cen sgRNA expressing cells, we frequently observed that in the presence of rapalog, at least two entire sister chromatid arms, lacking CENP-C, resided near the spindle pole(s) (Fig 7A and B). This suggests that only the q arms, on which dCas9 and Kin14VIb were bound, were transported toward the spindle pole(s). Moreover, instead of chromosomal arms sticking out from the metaphase plate, as observed when Kin14VIb is bound to the Chr1-telo loci (Figs 2A–D and 5C), we found that the sister chromatid 9q arms at the poles were connected to chromosomes in the metaphase plate by a stretch of dCas9-bound chromatin (Fig 7A). Our data suggest that while the 9q arms were transported toward the spindle poles by Kin14VIb attached to the pericentromeric region, the sister KTs of this chromosome congressed toward the metaphase plate, most likely via microtubule interactions. This could explain the absence of a mitotic delay despite visible poleward transport of Chr9-cen loci (Fig 6D). Since we observed stretching of Chr9-cen chromatin as early as metaphase, we anticipated that a stretch of pericentromeric heterochromatin might persist as a (fine) chromatin bridge during anaphase. Indeed, the unequal distribution of Chr9-cen induced by Kin14VIb binding was frequently accompanied by a stretch of H3S10ph$^+$ chromatin during anaphase that was often not detectable by DAPI (Fig 7C–F). We predict that these fine H3S10ph$^+$ chromatin bridges eventually resolve during telophase or later, resulting in an unequal distribution of the q arm over the daughter cells. In addition, the IF analysis revealed a segregation category where one of the targeted chromosomes is transported toward a spindle pole, but with (part of) the other Chr9 lagging ("2ss-1 + 1 lag," Fig 7C–F). We consider this the result of a prior "1 in, 1 out" metaphase orientation, with the aligned locus being incompletely replicated during S phase (Fig 7D, green dotted lines). In other words, one copy of Chr9 experienced the "background" segregation error that we observe in the absence of rapalog (Fig 7C–F).

Generation of 9q aneuploidies after a single cell division with Kin14VIb bound to Chr9

To reveal the fate of Chr9 after a round of Kin14VIb-induced mis-segregation, we single-cell sorted EdU$^+$ RPE1-dCas9-Kin14VIb G1 cells following an overnight incubation with rapalog and processed the cells for scKaryo-seq (Fig EV4A). As expected, the single-cell karyotype heatmaps of the near-diploid RPE1 cells were more homogeneous than those derived from U-2 OS cells (Figs 8A and EV2B). RPE1-dCas9-Kin14VIb cells displayed a clonal gain of Chr10q and Xq. While the gain of 10q is a clonal abnormality specific to RPE1 cells (Soto et al, 2017; Worrall et al, 2018), the gain of Xq arose during clonal selection required to derive the dCas9-Kin14VIb expressing cell line (Fig 8A). In addition to this, we selected for an infrequent gain of 19p, which appeared to increase after sgRNA transduction and Kin14VIb expression. Importantly, the rapalog-inducible FKBP12-FRB dimerization modality of our system allowed us to directly assess the effect of Kin14VIb motor binding to Chr9 on

the distribution of this chromosome after cell division. Indeed, we detected Chr9 copy number deviations in ~24% (25/105) of the cells treated with rapalog versus ~10% (4/39) of the cells that were not treated with rapalog (Fig 8A). Note that the efficiency of aneuploidy induction detected by scKaryo-seq is expected to be lower than the mis-segregation efficiency observed after microscopic inspection (Figs 6B and 7E and F) because (i) Kin14VIb-mediated chromosome transport efficiency is not identical in all cells and can vary per experiment, (ii) we cannot select for cells expressing the sgRNA, and (iii) the "2-2, same sisters" type of mis-segregation is unlikely to result in a copy number deviation and will be missed by scKaryo-seq.

Interestingly, the addition of rapalog increased the aneuploidy score of 9q (Fig 8B, Table EV2) and resulted in the loss and gain of both 9q homologs (9q nullisomy and tetrasomy, respectively, Fig 8C), as well as the frequent loss of one 9q homolog (monosomy of 9q, Fig 8C). The 9q monosomies were not accompanied by an increase in 9q trisomies, which we had expected based on our live- and fixed-cell imaging analyses (Figs 6 and 7). When following cells by live-cell imaging for longer times, we noted that in all Chr9-cen distribution categories, the mis-segregating 9q locus and arm occasionally formed a GFP-positive micronucleus in one or both daughter cells (in ~29% (+ rapalog) vs ~14% (−rapalog) of all the daughter cells, a GFP-positive MN was observed, Fig EV5A). In case of a 2-2ss, or 4-0 distribution of the 9q locus, most of these micronuclei originated from Kin14VIb-bound Chr9q arms that were misaligned in metaphase and remained polar during anaphase (Fig EV5A and B). In contrast, in the cases of a 3-1 distribution, or bridge/fragmentation, MN predominantly originated from lagging chromatin (Fig EV5A and B). Variations in locus distribution (i.e. 3-1 vs 4-0 and 2-2ss) and subsequent 9q fate most likely reflect differences in Kin14VIb-mediated chromosome pulling efficiency caused by variations in sgRNA expression levels per cell and per experiment after lentiviral transduction (Figs 6B and C, and 7F). Apparently, in the scKaryo-seq experiment, more divisions resulting in a 3-1 than a 4-0 locus distribution had taken place (Fig 8D). We argue that, despite sorting whole single G1 cells, DNA in MN may get lost during cell suspension and library preparation (Worrall et al, 2018), particularly when these MN originated from lagging chromatin, as the nuclear envelopes of these MN are considered to be more prone to rupture (Liu et al, 2018). Altogether, this may explain the bias for 9q monosomies in our scKaryo-seq results.

Next, we aimed to narrow down where chromosome 9 would break after Kin14VIb-induced mis-segregation. The initial results of the AneuFinder breakpoint refinement analysis suggested that for most of the cells the breakpoints are located roughly 10 Mb upstream from the pericentromeric repeat targeted by Chr9-cen sgRNAs (Fig EV4B, left panel). However, based on visual inspection of the results of individual cells, these estimates appeared to be off (Fig EV4B, right panel) and we therefore applied two different methods to obtain a better breakpoint estimate. First, a shifting breakpoint approach was implemented where the residual sum of squares (RSS) was calculated for different transitions (i.e., possible breakpoints) across the entire chromosome (Fig EV4C). This analysis predicted that for most cells, the breakpoint is just after the pericentromeric repeat (Fig EV4D, left panel). However, two bins overlapping the pericentromeric repeat were excluded from this analysis (Fig EV4B and D, right panels, red dots). These bins
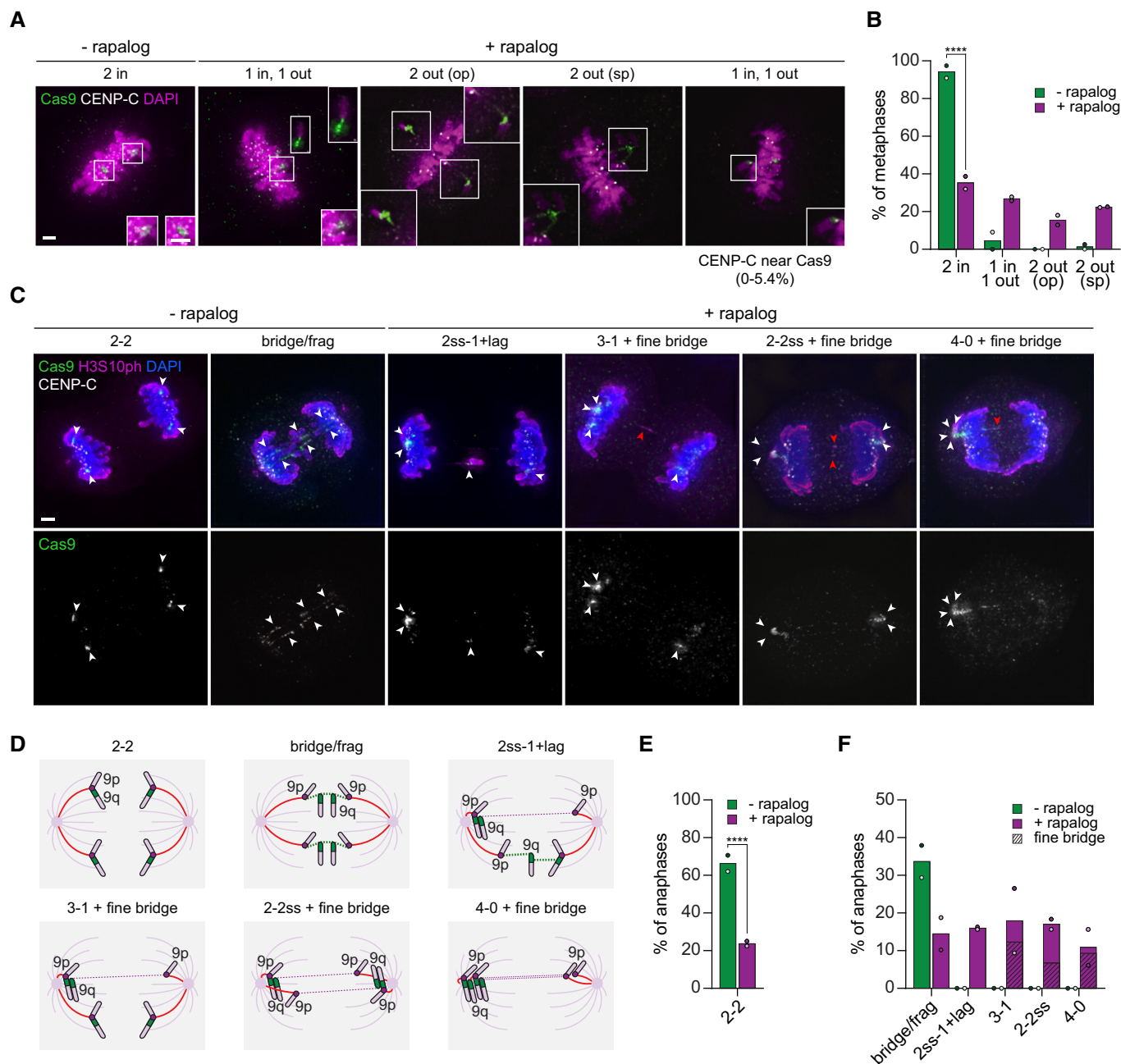
Figure 7. Segregation errors induced after Kin14IVb tethering to Chr9.

A Representative IF images of RPE1-dCas9-Kin14VIb cells, showing the localization of the Chr9-cen loci in metaphase in the absence or presence of rapalog. Magnifications of the white boxed regions (each region showing one Chr9-cen locus) are shown in the corners (scale bars = 2 μm). The fraction of cells with Chr9 misaligned and CENP-C near the locus (Cas9) is indicated below the image. For clarity, the maximum intensity projection of a subset of z stacks in which the Chr9-cen loci are in focus (2–10/100) is shown.

B Frequency of the observed metaphase localizations of the Chr9-cen loci as shown in (A).

C Representative IF images of RPE1-dCas9-Kin14VIb cells, showing the segregation and distribution of Chr9-cen loci in anaphase (white arrowheads). Red arrowheads indicate H3S10ph-positive chromatin bridges. For clarity, the maximum intensity projection of a subset of z stacks in which the chr9-cen loci are in focus (30–62/100) is shown. Scale bar = 2 μm.

D Schemes illustrating the correct and incorrect segregation of Chr9-cen locus and arms, based on (C).

E Frequency of cells with a 2-2 distribution of the Chr9-telo loci.

F Frequency of the observed segregation/distribution errors of the Chr9-cen loci as shown in (C).

Data information: In all cases, bars represent the mean of 2 independent experiments, while dark- and light-colored dots represent the values of each experiment. (B): ****$P < 0.0001$, Fisher's exact test. $N \geq 31$ cells per condition, per experiment. (E, F): ****$P < 0.0001$, Fisher's exact test. $N \geq 29$ cells per condition, per experiment. (A, C): For optimal visibility of the Chr9-cen foci H3S10ph-positive chromatin bridges, the brightness and contrast of all channels were linearly adjusted for individual cells.

showed aberrant read counts, which have a substantial influence on the calculation and can result in incorrect breakpoint estimates. Because of this limitation, we also implemented a noninteger copy number calculation, which includes these bins, and estimates the *average* breakpoint location of all cells with a Chr9q gain or loss (Fig EV4E). The first bin that showed a significant difference in copy number between cells without and with a 9q gain or loss was the first bin (Bin 1) after the centromere bin (Bin 0). This bin has a large overlap with the pericentromeric repeat. In addition, Bin 0 already showed some difference, although not statistically significant ($P = 0.05833$; Fig EV4E). These results suggest that, on average, the breakpoint is located close to the centromere, and within the
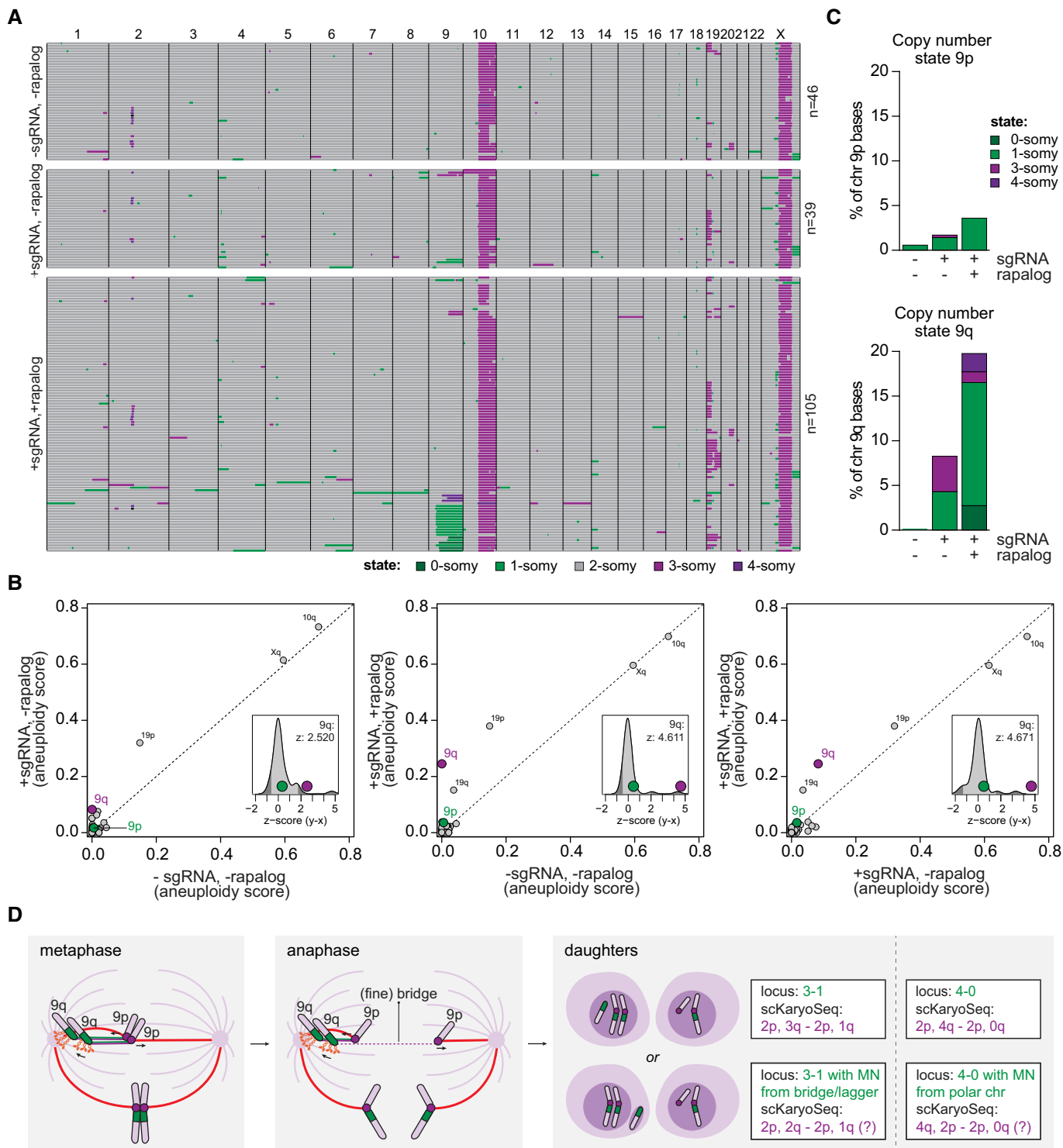

Figure 8.

◀

Figure 8. Tethering Kin14VIb to a pericentromeric DNA repeat in Chr9 results in 9q aneuploidies after a single cell division.

A   Genome-wide copy number heatmaps of RPE1 dCas9-Kin14IVb cells for the indicated conditions. Note that in the -sgRNA condition, Kin14IVb is not expressed (−dox), while in the +sgRNA conditions, the kinesin is expressed (+dox). Individual cells are presented in rows and genome positions in columns. Chromosome boundaries are indicated with black lines and colors correspond to the most probable copy number states per bin as determined by AneuFinder.

B   Plots comparing aneuploidy scores for each chromosomal arm between the various indicated conditions. The aneuploidy scores of the chromosomal arms are deviations from euploid (average absolute difference from 2-somy of the bins that are associated with the arm). Inserts show density plots of the difference of the scores of the two conditions that are compared (y-axis minus x-axis). These differences are expressed as z-scores (number of standard deviations from the mean). The 95% confidence interval is depicted in light gray. The values of the 9p and 9q arm are indicated with a green and purple dot, respectively. Z-score value for 9q is indicated (see also Table EV2).

C   Average percentage of the bases of the p or q arm that are (classified as) 0, 1, 3 or 4-somy. Percentages are depicted as stacked bar plots and are determined for all copy numbers other than 2-somy (euploid).

D   Scheme illustrating how Kin14VIb binding to an endogenous pericentromeric repeat in Chr9q may cause Chr9 arm-level aneuploidies after a single cell division. For clarity, only the situation where one Chr9 homolog is at the pole during metaphase is drawn.

pericentromeric repeat region of 9q12, in line with our predictions based on the fixed and live-cell imaging results (Figs 6 and 7). Taken together, our data suggest that targeting Kin14VIb to endogenous repetitive loci on single chromosomes is a powerful means to induce chromosome-specific mis-segregations that result in arm-level aneuploidies after a single cell division (Fig 8D).

Discussion

We here demonstrate the feasibility of manipulating the orientation and segregation of specific human chromosomes during mitosis by recruiting the minus-end-directed Kin14VIb of *P. patens* to chromosome-specific repetitive loci. Interestingly, in maize, the so-called abnormal chromosome 10 (Ab10) harbors a cluster of eight genes, known as the Kinesin driver (Kindr) complex, that promotes meiotic drive, that is, the preferential transmission of Ab10 into egg cells (Dawe *et al*, 2018). The mechanism of Ab10 drive involves the conversion of inert heterochromatic regions called knobs into motile "units" that are actively transported along microtubules toward spindle poles during meiosis I and II (Yu *et al*, 1997). It was recently demonstrated that Ab10 knob transport is mediated by Kindr encoded KINDR, a minus-end-directed motor protein that diverged from a Kinesin 14A ancestor and specifically interacts with 180-bp knob repeats (Dawe *et al*, 2018). Through rTetR and dCas9-mediated tethering of *Pp* Kin14VIb to subtelomeric and pericentromeric heterochromatic repeats, we appear to have mimicked this chromosomal "drive" mechanism in human mitotic cells, forcing unequal transmission of targeted chromosomal arms into daughter cells.

We find that the accumulation of Kin14VIb dimers on a highly repetitive (∼ 200 × 96mer) integrated TetO locus induces poleward transport of the TetO locus in U-2 OS cells (Janicki *et al*, 2004), causing the tethered chromosome 1p arm to be pulled toward the spindle pole. We noted, however, that GCN4-induced Kin14VIb tetramers are more effective in chromosome transport than Kin14VIb dimers, when employing dCas9 to tether the motor to endogenous Chr1p36-specific DNA repeats. The lower number of sgRNA binding sites (∼1,400 in the endogenous repeats compared to ∼19,200 rTetR-binding sites in the integrated TetO repeat) will likely result in a smaller number of dCas9 and hence Kin14VIb molecules to accumulate on the endogenous locus, thereby affecting the probability of the dimeric motor to dimerize (Jonsson *et al*, 2015; Yamada *et al*, 2017). Moreover, in RPE1 dCas9-Kin14VIb cells, Kin14VIb is not

fused to dCas9. Instead, the two proteins are separately expressed and coupled to each other via rapalog-inducible heterodimerization of FRB (fused to the Kin14VIb) and FKBP12 (fused to dCas9). Cellular factors, such as endogenous FKBP12 protein levels and the amount of sgRNA expressed per cell, will impact the efficiency of Kin14VIb recruitment to the locus of interest after rapalog addition (Ballister *et al*, 2014). For these reasons, the number of Kin14VIb motors binding to a particular locus in RPE1 dCas9-Kin14VIb cells is likely to be lower than predicted.

Kin14VIb tethering to either subtelomeric or pericentromeric loci was compatible with microtubule attachment to the KTs of the targeted chromosome. When tethered to a subtelomeric repeat in Chr1p, it allowed the acquisition of bioriented MT attachments by the sister kinetochores that facilitated sister KT congression. Although we frequently observed poleward orientation of the Kin14VIb bound loci after NEB, it is possible that MT capture of the respective KTs is even faster and was already established before Kin14VIb began transporting the telomere toward the spindle pole. Alternatively, Kin14VIb-mediated telomere transport may have started before the kinetochores acquired MT attachments, for instance because at NEB the TetO chromosome was in close proximity of one of the spindle poles. We propose that the latter scenario might explain the observed mitotic delay in the cells where the TetO locus was initially pulled toward one of the spindle poles, but segregated equally during anaphase (i.e., the "out to 1-1" group). We speculate that in this scenario, the movement of the ends of the Chr1 sister p arms toward the spindle pole might affect the back-to-back orientation of sister KTs, or unfavorably position the TetO chromosome behind the spindle pole, a condition that was recently described to delay chromosome alignment (Klaasen *et al*, 2022). However, once amphitelic end-on attachments are established, the pulling forces applied by the KT-bound MTs (kMTs) will counteract the poleward forces exerted by Kin14VIb at the TetO locus near the telomere. Depending on the number of Kin14VIb molecules present on the TetO locus, this kMT pulling force could lead to detachment of the Kin14VIb motors from MTs, resulting in a 1-1 segregation of the TetO locus. Finally, even when Kin14VIb was bound to the large pericentromeric repeat of Chr9q, one or two of the nearby sister KTs could attach to MTs derived from the opposing spindle pole, causing the pericentromeric heterochromatin to stretch and spatially separate from the kinetochore during metaphase.

The opposing forces exerted by Kin14VIb and kinetochore MTs on the same chromosome had striking consequences for the

segregation of that chromosome during anaphase. When bound close to the telomere of Chr1, Kin14VIb caused the p arm to stretch heavily when the KT of the sister chromatid was connected to MTs derived from the opposing spindle pole, revealing the plasticity of a human mitotic chromosome under physiological conditions, that is, in living cells. The increase in Chr1p aneuploidy scores deduced from scKaryo-Seq of individual U-2 OS nuclei implies that the stretched 1p arm is eventually broken and gained in, or lost from the daughter nuclei. Since we did not detect γH2AX on the bridges during late anaphase, we consider it likely that, similar to chromatin bridges formed by dicentric chromosomes as a consequence of telomere fusions, the 1p arm gets trapped and damaged in the intercellular cytokinetic bridge during (late) telophase. Future work will show if breakage of the 1p arm involves the action of the endonuclease TREX1, or if it is mediated by actomyosin forces as described for bridges formed by dicentric chromosomes (Janssen *et al*, 2011; Maciejowski *et al*, 2015; Umbreit *et al*, 2020). When bound to pericentromeric repeats of Chr9q close to the sister KTs, the opposing pulling forces exerted by kMTs and Kin14VIb appeared to stretch part of the pericentromeric heterochromatin, separating the sister q arms from the p arms and kinetochores during metaphase and anaphase, often accompanied by a fine, H3S10ph-positive chromatin bridge. Whether spindle forces are sufficient to break these (fine) heterochromatin bridges remains to be determined. However, breakpoint analysis of our scKaryo-Seq data revealed that breakage indeed occurs in the pericentromere repeat of 9q to which Kin14VIb is targeted, thus leading to 9q gains and losses in the daughter cells.

Opportunities and limitations of the approach

We developed an approach to enable both the visualization and manipulation of specific chromosomes during mitosis and that induced chromosome-specific segmental aneuploidies in daughter cells after one round of cell division. In an accompanying article, Tovini *et al* employed dCas9-CENP-T fusion proteins to build an ectopic kinetochore on targeted chromosomes, a strategy that also increased the frequency of chromosome-specific CIN and aneuploidies (Tovini *et al*, 2023). In addition, Bosco *et al* developed an elaborate computational pipeline to analyze the T2T human genome assembly for sgRNAs binding to chromosome-specific centromere-repeats (Bosco *et al*, 2023; Nurk *et al*, 2023). These sgRNAs were used to tether a dCas9-GFP-Knl1[1-86/RVSFmut] fusion protein onto centromeres, a strategy that resulted in both segmental and whole-chromosome-specific aneuploidies of various chromosomes (Bosco *et al*, 2023). These three novel approaches rely on nuclease-dead Cas9 and one unique sgRNA to tether a protein-of-interest to a chromosome-specific highly repetitive sequence; sequences that are predominantly found in subtelomeric or (peri-)centromeric chromosomal regions (Bosco *et al*, 2023; Tovini *et al*, 2023). Earlier methods employed nuclease-active Cas9 to delete an entire mouse or human chromosome by inducing DNA double-strand breaks in centromeres or along a chromosomal arm using multiple unique sgRNAs (Adikusuma *et al*, 2017; Zuo *et al*, 2017). In addition, the deletion of a specific chromosomal arm was accomplished by combining CRISPR-Cas9-induced fragmentation of a chromosomal arm with the recombination of an artificial telomere (Taylor *et al*, 2018). Although highly creative and powerful, these Cas9-based methods can only generate chromosomal losses but not gains. Moreover,

clonal expansion is required before further analysis of the resultant aneuploid cells is possible, making these approaches unsuitable to study the immediate consequences of specific aneuploidies. More recently, Leibowitz *et al* demonstrated that a single cut by CRISPR-Cas9 can also generate on-target chromosome bridges and the formation of micronuclei, leading to massive rearrangement (chromothripsis) of the targeted chromosome (Leibowitz *et al*, 2021). While useful to study the consequences of chromosome-specific MN entrapment and subsequent chromothripsis, the percentage of MN that formed was relatively low (< 10%, vs. 29% of daughter cells containing a MN with known content with our system), making it challenging to isolate (grand)daughter cells with on-target chromothripsis.

The employment of nuclease-dead Cas9 fused to GFP and FKBP12 renders our method versatile and useful in several ways. First, it allows tracking of the targeted loci over time and the visualization of their unequal distribution over daughter cells caused by the FKBP12-bound FRB-Kin14VIb. This paves the way to analyze responses and phenotypic changes in the daughter cells by correlative live imaging and multiplex immunofluorescence (Gut *et al*, 2018; Dumont *et al*, 2020). Moreover, when combined with microscopy-based single-cell isolation methods and subsequent sequencing, such as described for Look-Seq (Zhang *et al*, 2015), Live-Seq (Bollen *et al*, 2021), or Photostick (Chien *et al*, 2015), our system offers the potential to study the immediate cellular responses to a specific (arm-level) gain and loss in different cell types in an unbiased manner; an important step toward understanding how recurrent aneuploidy patterns arise in different cancer types. Second, we can target Kin14VIb to different chromosomes and to different chromosomal regions. When taking the number of sgRNA binding sites for Chr1-telo (~1,400) as reference (see also discussion below), our motor-based strategy would in theory be suitable for the subtelomere of chromosome 15, the pericentromere of chromosomes 1, 2, 7, 9, and 16, and the centromere of chromosomes 1, 2, 4–12, 17–19, and X (Bosco *et al*, 2023; Tovini *et al*, 2023). Third, by taking advantage of the poleward pulling forces exerted by Kin14VIb on the targeted chromosome, our method can also be applied to study biophysical properties of mitotic human chromosomes in living cells.

Importantly, however, the use of dCas9 also has its limitations. When comparing the Kin14VIb-dependent minus-end-directed transport efficiency of Chr9-cen to Chr1-telo loci in our dCas9-Kin14VIb RPE1 cell line, we observed that the number of sgRNA binding sites matter because the Chr9-cen sgRNA performed better than the Chr1-telo sgRNA. This is most likely because more dCas9 molecules, and hence more motor proteins, accumulate on the large repeat of Chr9q (~ 550,000 sgRNA binding sites) than on the smaller Chr1p repeat (~ 1,400 sgRNA binding sites). Thus, an important success criterium for our approach, as well as the other recent dCas9-based strategies (Bosco *et al*, 2023; Tovini *et al*, 2023), is the presence of a large number of unique sgRNA binding sites on a chromosome of interest. Based on our experience with the Chr1-telo sgRNA, we consider ~ 1,400 binding sites a minimal requirement for our motor-based strategy. At the same time, the binding of many dCas9 molecules to a repetitive stretch of DNA runs the risk of hampering timely replication of these repeats during S phase, which in turn may result in DNA bridges and damage during anaphase and telophase, respectively (Whinn

et al, 2019; Doi *et al*, 2021). The fact that we observed GFP-positive bridges during anaphase in ∼ 30% of the RPE1-dCas9-Kin14VIb cells transduced with the Chr9-cen sgRNA, but without Kin14VIb binding to the repeat, underscores this notion. We consider it likely that the mere binding of dCas9 to the recently published centromere-specific repeats induces similar replication issues (Bosco *et al*, 2023). Importantly, the inducible FKBP12-FRB dimerization modality and the presence of a NES in Kin14VIb enabled a direct assessment of the consequence of Kin14VIb motor binding to a chromosome of interest during mitosis. We found that binding of Kin14VIb to Chr9-cen enhances the mis-segregation rate of Chr9q over the dCas9-induced background rate by causing typical 9q misalignments that are not caused by prior replication issues. Moreover, the engineering of an S-phase degradable dCas9 through for instance fusion of dCas9 to a specific N-terminal part of the chromatin licensing and replication protein 1 (Cdt1; Howden *et al*, 2016; Sakaue-Sawano *et al*, 2017) could be a viable future strategy to avoid replication issues caused by mere dCas9 binding to a repetitive locus of interest.

Because in our hands the visualization and tracking of chromosomal loci in living cells was hampered by high expression levels of dCas9-GFP, we used a weak UBC promotor to drive dCas9 expression (Dumont *et al*, 2020). Bosco *et al*, however, find that high expression levels of dCas9 improve the efficiency of aneuploidy induction (Bosco *et al*, 2023). Hence, our efforts to generate a system that allows both the manipulation *and* tracking of a targeted chromosome by live-cell imaging may have accidently selected for suboptimal efficiency of generating aneuploidies. Finally, after targeting Kin14VIb to either subtelomeric or pericentromeric repeats, we predominantly generated chromosome-specific segmental aneuploidies. Since the immediate and long-term cellular responses to and consequences of either segmental or whole-chromosome aneuploidies can be different at least in RPE1 cells (Santaguida *et al*, 2017; Soto *et al*, 2017; Hintzen *et al*, 2022), improving our method to induce whole-chromosome-specific CIN and aneuploidies remains relevant. The recently predicted sgRNAs that target unique centromeric repeats (Bosco *et al*, 2023; Tovini *et al*, 2023) allow docking of Kin14VIb directly on the centromere. How the accumulation of an excess of minus-end-directed Kin14VIb motors on the centromere would affect targeted chromosome congression, KT-MT attachment acquisition, and segregation fidelity during anaphase, and whether this would favor the mis-segregation of a whole chromosome instead of chromosomal arms remain important topics for future studies.

Materials and Methods

Cells and cell culture

HEK293T cells were cultured in DMEM (Sigma-Aldrich) medium. U-2 OS TetO (Janicki *et al*, 2004) and all hTERT-RPE1 cell lines (referred to as RPE1) were cultured in DMEM-F12 medium (Sigma-Aldrich). Medium was supplemented with 10% fetal bovine serum (Bodinco B.V.), 1 mM ultraglutamine (Lonza), and 0.1 mg/ml penicillin/streptomycin (Sigma-Aldrich). Cells were cultured at 37°C and 5% CO_2 in a humidified incubator.

Plasmids

The lentiviral vector F9-rTetR-EGFP-IRES-PuroR was generated by Gibson cloning from F9-TetR-EGFP-IRES-PuroR (gift from Huimin Zhao, Addgene plasmid # 117049). TetR was replaced by reverse (r) TetR obtained by PCR from AAVS1 TRE3G-GFP (gift from Su-Chun Zhang, Addgene plasmid # 52343). *Pp*Kin14VIb cDNA was obtained by PCR from pSIN-TRE-rtTA-IRES-Puro-FRB-mCherry-GCN4-*Pp*Kin14VIb and cloned into F9-rTetR-EGFP-IRES-PuroR to generate F9-rTetR-EGFP-*Pp* Kin14VIb-IRES-PuroR. pSIN-TRE-rtTA-IRES-PuroR-FRB-mCherry-GCN4-*Pp*Kin14VIb (861-1321) was constructed from pSIN-TRE-rtTA-IRES-Puro (kindly provided by Benjamin Bouchet, Utrecht University, The Netherlands), and encodes tetramerized GCN4- *Pp* Kin14VIb (aa 861-1321), derived from the plasmid *Pp*Kin14VIb–GCN4, a gift from Gohta Goshima (Nagoya University, Nagoya, Japan), and was fused N-terminally to the rapalog-sensitive heterodimerization module FRB and mCherry.

pSIN-TRE-rtTA-IRES-PuroR-FRB-mCherry-GCN4-*Pp*Kin14VIb (861-1321) is a self-inactivating lentiviral vector enabling doxycycline-sensitive expression of the minus-end-directed kinesin FRB-mCherry-GCN4-*Pp*Kin14VIb (861-1321), carrying a puromycin resistance cassette and the reverse tetracycline-controlled transactivator, rtTA.

To generate the lentiviral vector pCuO-rTetR-EGFP, rTetR-EGFP was amplified by PCR from F9-rTetR-EGFP-IRES-PuroR and cloned into pCDH-CuO-MCS (SystemBio, cat. no. QM500A-1) by Gibson assembly. Human codon-optimized *Pp*Kin14VIb (Integrated DNA Technologies) was subsequently cloned into pCuO-rTetR-EGFP to generate pCuO-rTetR-EGFP-*Pp*Kin14VIb.

The lentiviral vector pHAGE-UbC-dCas9-GFP-3xFKBP was generated from pHAGE-TO-dCas9-3xGFP, a gift from Thoru Pederson (Addgene plasmid # 64107). By Gibson cloning, the final 2xGFP were replaced by 3xFKBP, obtained by PCR from pcDNA5 FKBP-GFP (a gift from Geert Kops, Hubrecht Institute, the Netherlands). The Chr1-telo (sequence: GATGCTCACCT) and Chr9-cen (sequence: TGGAATGGAATGGAATGGAA) sgRNAs were selected based on the principles described in Ma *et al*, 2015, and cloned into lentiviral vector pLH-spsgRNA2 (gift from Thoru Pederson, Addgene plasmid # 64114). The Chr1-telo sgRNA was described in Dumont *et al*, 2020.

For CRISPR/Cas9 knockout of the puromycin N-acetyl-transferase (PAC) gene in RPE1 cells, the sgRNA GGCGGGGTAGTCGGCGAACG was cloned into the expression vector pAceBac1-U6-CBA-Cas9-2A-EGFP, generated as described previously (Hindriksen *et al*, 2017).

Lentivirus production and transduction

For lentivirus production, HEK293T cells were seeded in 10 cm dishes at 10% confluency 24 h prior to transfection. Cells were co-transfected with lentiviral vectors plus the lentiviral packaging and envelope plasmids: psPAX2 (Addgene plasmid #12260) and psMD2.G (Addgene plasmid #12259). Lentivirus containing FRB-mCherry-GCN4-Kin14VIb and rTetR-GFP-Kin14VIb was harvested by filtering the cell supernatant through a 40 μm filter at 48- and 72-h post-transfection. Filtered cell supernatants were incubated in a 5× concentrating solution consisting of 400 g/l PEG 6000 and 0.41 M NaCl (pH 7.2) at 4°C overnight. The supernatant and concentrating solution mixture was centrifuged at 4,415 *g* for at least 30 min, resuspended in 100 μl ice-cold PBS, and stored at −80°C until transduction. Lentivirus containing dCas9-GFP-3xFKBP, rTetR-

GFP, Chr1-telo sgRNA, and Chr9-cen sgRNA were harvested 48-h post-transfection as described previously and stored at −80°C until transduction. For lentiviral transduction, cells were seeded at 30–40% confluency in a 6-well plate and incubated for 16–24 h with lentivirus containing FRB-mCherry-GCN4-Kin14VIb or rTetR-GFP-Kin14VIb, Chr1-telo or Chr9-cen sgRNAs, and dCas9-GFP-3xFKBP or rTetR-GFP, respectively, in the presence of 6 µg/ml polybrene.

Cell line generation

To generate RPE1 cell lines stably expressing dCas9-GFP-3xFKBP, RPE1 cells were transduced with lentivirus containing dCas9-GFP-3xFKBP and after a week were sorted for low GFP expression by flow cytometry. Subsequently, RPE1 cells stably expressing dCas9-GFP-3xFKBP were transduced with lentivirus containing FRB-mCherry-GCN4-Kin14VIb. A population of high mCherry-Kin14VIb-expressing cells was obtained by flow cytometry, expanded in culture, and plated as single cells into 96-well plates containing 100 puromycin-sensitive feeder RPE1 cells. Puromycin-sensitive RPE1 cells were generated by CRISPR-Cas9 mediated mutation of the puromycin N-acetyl-transferase (PAC) gene. Seven days after plating, feeder cells were eliminated by puromycin selection (1 µg/ml, Sigma-Aldrich). Expanded clones were transduced with lentivirus containing Chr1-telo sgRNA and treated for 16 h with 20 µM of the Eg5 inhibitor S-trityl-L-Cysteine (STLC, Tocris Biosciences) to generate a population of mitotic cells with monopolar spindles. Cells were then treated with 500 nM rapalog (AP21967/AC heterodimerizer, Clontech) to induce FKBP12-FRB dimerization and were followed by live-cell imaging. The clone with the largest fraction of cells showing polar localization of Chr1-telo GFP foci after rapalog addition was selected for further experiments. This cell line is referred to as RPE1 dCas9-Kin14VIb.

Live-cell imaging

U-2 OS TetO cells stably expressing H2B-mCherry were transduced with lentivirus containing rTetR-GFP or rTetR-GFP-Kin14VIb. Nine-day post-transduction, cells were seeded in an optical-quality plastic 8-well slide (IBIDI, cat. no. 80826) for live-cell imaging. The next day, media were replaced by FluoroBrite DMEM (Gibco) supplemented with 10% fetal bovine serum (Bodinco B.V.), 1 mM ultra-glutamine (Lonza), and 0.1 mg/ml penicillin/streptomycin (Sigma-Aldrich). Cells were treated with 1 µg/ml doxycycline to induce TetO-rTetR binding prior to live-cell imaging. Images were acquired every 5 min on a Zeiss AIM System—Cell Observer microscope equipped with an AxioImager Z1 stand, a Hamamatsu ORCA-flash 4.0 camera, and a Colibri 7 LED module, using a 40×/1.4 oil PLAN Apochromat lens. All movies were subsequently processed and analyzed using ZEN software (Zeiss).

RPE1 dCas9-Kin14VIb cells were transduced with lentivirus containing Chr1-telo or Chr9-cen sgRNAs. 24 h after transduction, cells were plated for live-cell imaging in an optical-quality plastic 8-well slide (IBIDI, cat. no. 80826). The next day, cells were incubated with 200 nM SiR-DNA (Spirochrome) and 1 µg/ml doxycycline to visualize DNA and induce FRB-mCherry-Kin14VIb expression, respectively. After 8 h, cells were treated with 500 nM rapalog (Clontech) to induce FRB-FKBP dimerization, and images were acquired every 5 min on a Zeiss AIM System—Cell Observer microscope as described previously.

Chromosome spreads

For chromosome spread preparations, cells were synchronized in mitosis by a 16-h incubation in 20 µM STLC (Tocris Biosciences). Following a 10-min treatment with 0.83 µM nocodazole (Sigma-Aldrich), mitotic cells were harvested by shake-off and incubated in 75 mM KCl for 10 min. Subsequently, cells were spun onto glass coverslips in a Cytospin centrifuge at 378 g for 5 min. Samples were fixed and stained as described below.

Cell synchronization and immunofluorescence

U-2 OS TetO cells were transduced with lentivirus containing rTetR-GFP or rTetR-GFP-Kin14VIb. 7-day post-transduction, cells were plated on coverslips and incubated overnight in 7 µM RO-3306 (Sigma-Aldrich) to synchronize in G2 phase of the cell cycle. The next day, for anaphase synchronization, cells were washed 3× with warm media to release from RO-3306 and incubated for 1 h in medium containing 1 µg/ml doxycycline to induce TetO-rTetR binding, prior to fixation. Alternatively, cells were synchronized in metaphase by a 20 min RO-3306 release in the presence of 1 µg/ml doxycycline, followed by a 45 min block in 5 µM MG132 (Calbiochem). RPE1 dCas9-Kin14VIb cells were transduced with lentivirus containing Chr1-telo or Chr9-cen sgRNAs and 24 h later plated in an optical-quality plastic 8-well slide (IBIDI, cat. no. 80826) for immunofluorescence. To induce Kin14VIb expression, RPE1 cells were treated with 1 µg/ml doxycycline for 16 h, followed by 4 h of treatment with 500 nM rapalog to induce binding of Kin14VIb to dCas9. Additionally, for screening of Kin14VIb efficiency, RPE1 cells were treated with 20 µM STLC and doxycycline simultaneously.

All samples were fixed in 4% PFA for 10 min and permeabilized with ice-cold methanol for at least 10 min, unless otherwise stated. For Mad1 IF, U-2 OS TetO cells were plated onto poly-D-Lysine-coated coverslips, synchronized in metaphase as described above, then fixed, and permeabilized simultaneously in 4% PFA diluted in PHEM-Triton buffer (60 mM HEPES, 20 mM Pipes, 10 mM EGTA, 2 mM MgCl$_2$, 0.2% Triton X-100, pH 6.9). Fixed samples were blocked in 3% BSA solubilized in PBS containing 0.1% Tween 20, incubated with primary antibodies for 2 h, washed, and incubated with secondary antibodies and 1 µg/ml DAPI (Sigma-Aldrich) for 1 h. For γH2AX IF, samples were fixed in 4% PFA for 15 min and incubated in PBS-Triton X-100 (0.5%) for 10 min to retrieve antigens. Blocking was performed in 2.5% BSA solubilized in PBS-Tween-20 (0.05%) for 15 min, and samples were incubated with primary antibodies at 4°C overnight. Secondary antibody incubation was performed for 2 h at room temperature, and 1ug/ml DAPI was used to visualize DNA in all samples. The following primary antibodies were used: GFP booster (Chromotek, gba488), mouse anti-γH2AX (Millipore 05-636), mouse anti-H3S10ph (Millipore, 05-806), rabbit anti-H3S10ph (Millipore, 06-570), guinea pig anti-CENP-C (MBL, PD-030), mouse anti-Mad1 (Millipore, MABE867), rabbit anti-pericentrin (Abcam, ab4448), mouse anti-Cas9 (Diagenode, C15200203), and rabbit anti-RFP (Rockland, ROCK600-401-379). Coverslips were mounted with Prolong Diamond (Invitrogen), and all samples were imaged with an inverted 100x oil objective on an Olympus IX71 microscope connected to a Deltavision imaging system and a CoolSnap HQ camera (Photometrics). For most images of fixed cells z steps of 0.2 µm were taken, except for image acquisition

of fixed RPE1 cells in ibidi chambers, where z steps of 0.1 μm were taken. All images shown are maximum projection of multiple z stacks after deconvolution by Softworx, unless otherwise stated. For quantification of mCherry and GFP fluorescence intensities from IF images, an ImageJ macro was applied to threshold on mCherry/GFP channels, and measure mean fluorescence intensities of both the threshold area and the background outside. Background values were then subtracted from the mean fluorescence values to obtain plotted values.

FISH

U-2 OS TetO cells were transduced with lentiviruses containing rTetR-GFP or rTetR-GFP-Kin14VIb, replated at 60% confluency 48-h post-transduction and incubated in 7 μM RO-3306 overnight. The next day, cells were washed 3× with warm media and incubated 1 h in medium containing 1 μg/ml doxycycline to induce TetO-rTetR binding, prior to fixation. Cells were fixed in ice-cold methanol:acetic acid (3:1) for 10 min at −20°C, and FISH using Chromosome 1 Classical Satellite Probe (LPE001R, Cytocell) was performed according to manufacturer's instructions. Samples were then incubated with 10 μl Antifade DAPI 0.125 μg/ml (Cytocell) for 10 min, before being mounted on glass slides and sealed using Rubber solution glue (Cytocell). All samples were imaged with an inverted 100x oil objective on an Olympus IX71 microscope connected to a Deltavision imaging system and a CoolSnap HQ camera (Photometrics). Z steps of 0.2 μm were taken for all FISH images. All images shown are maximum projection of multiple unprocessed (not deconvolved) z stacks, in which the FISH signals were in focus.

Single-cell karyotype sequencing

U-2 OS TetO cells were transduced with lentiviruses containing rTetR-GFP or rTetR-GFP-Kin14VIb. After 48 h, cells were replated at 60% confluency and incubated in 7 μM RO-3306 for 16 h. Cells were washed 3x with warm media and incubated in medium containing 1 μg/ml doxycycline to induce TetO-rTetR binding. Four hours after RO-3306 release, single nuclei were extracted by incubating cells on ice for at least 15 min in nuclei suspension buffer (NSB) containing 0.1 M Tris–HCl pH 7.5, 0.154 M NaCl, 1 mM CaCl$_2$, 0.5 mM MgCl$_2$, 0.2% BSA, 0.1% NP40, and 1 μg/ml Hoechst 34580 (Sigma-Aldrich).

RPE1 dCas9-Kin14VIb cells were transduced with lentivirus containing chr9-cen sgRNAs. After 36 h, cells were treated with 1 μg/ml doxycycline to induce FRB-mCherry-GCN4-Kin14VIb expression. Eight hours after doxycycline addition, cells were replated into a 6-well plate at a density of 170,000 cells/ml and incubated with 5 μM EdU (Thermofisher) ± 500 nM Rapalog (Clontech) for 17 h.

Cells were then fixed using 70% ice-cold ethanol, washed with 1× Saponin-based permeabilizing and washing reagent (Thermofisher), and incubated for 30 min with the Click-iT reaction cocktail according to the manufacturer's protocol (Thermofisher). Afterward, cells were washed with 1× Saponin-based permeabilizing and washing reagent, and DNA was stained using 1 μg/ml DAPI (Sigma-Aldrich).

Single nuclei or single cells were filtered through 40 μm strainers and sorted into 384-well plates containing 5 μl mineral oil (Sigma-Aldrich). Samples were further processed as described previously (Bolhaqueiro et al, 2019). Libraries of U-2 OS TetO and RPE1 cells were sequenced on an NovaSeq6000 S1 2 × 100 bp (80 M reads/384 single cells) and NovaSeq6000 S1 1 × 100 bp (67 M reads/384 single cells) sequencer, respectively. The fastq files were mapped to GRCH38 using the Burrows–Wheeler aligner. The aligned read data (bam files) were analyzed with a copy number calling algorithm called AneuFinder (version 1.14.0; Bakker et al, 2016). Following GC correction and blacklisting of artifact-prone regions (extreme low or high coverage in control samples), libraries were analyzed using the dnacopy and edivisive copy number calling algorithms with variable width bins (average binsize = 1 Mb; step size = 500 kb). Breakpoints were refined as well (refine.breakpoints = TRUE). The samples were analyzed with an euploid reference (van den Bos et al, 2016). Results were afterward curated by requiring a minimum concordance of 90% between the results of the two algorithms. Libraries with on average less than 10 reads per bin and per chromosome copy (~55,000 reads for a diploid genome) were discarded. The DNA copy results are presented. The copy numbers of the U-2 OS TetO samples were expressed relative to the median (consensus) copy number profile of the nontransduced U-2 OS TetO cells ("non-transduced") in order to account for the noneuploid nature of this cell line (see Fig EV2B). This median copy number was determined for each bin (median across libraries). Aneuploid scores were first calculated for each bin by calculating the average absolute difference from this median copy number profile (average across libraries). Scores for chromosomal arms were subsequently calculated by averaging the scores of the bins that were associated with each arm (weighted average; bins have variable width). The aneuploidy scores of the RPE1 samples were calculated in the same way except that the scores were calculated relative to an euploid reference (absolute difference from 2-somy).

Chromosome breakpoint analysis

Two different methods were implemented for estimation of the breakpoints on chromosome 9. The first method uses a shifting breakpoint approach where all possible breakpoints (every transition between bins) were tested by calculating the residual sum of squares (RSS). The RSS is calculated each time as the sum of the squared differences between the read count of each bin, and the average bin read count of the state it is assumed to belong to (mean of the state; Fig EV4C). The transition that gives the smallest RSS is assumed to be the true position of the breakpoint. The second method tests for differences in copy number between cells with a gain of one or two q arms and cells with a loss of one or two q arms. Cells were divided into three groups: (i) cells that gained one or two q arms, (ii) cells that lost one or two q arms, and (iii) cells that were not affected. We subsequently went back to the original read counts of the bins, and calculated noninteger copy numbers for each bin and each cell (instead of copy numbers for segments as is done by AneuFinder). This calculation was performed by dividing the observed bin read count by the average number of reads per bin of the 2-somy state (mean 2-somy) divided by two (to get the number of reads per copy; denominator):

$$\text{Non} - \text{integer copy number bin} = \frac{\text{Observed read count bin}}{\text{Mean 2} - \text{somy state 1} 2}$$

Finally, for bins around the pericentromeric repeat, a Wilcoxon rank-sum test was used to test for differences between the cells that either gained one or two 9q arms or lost one or two 9q arms. Importantly, the original coordinates of the pericentromeric repeat targeted by Chr9-cen sgRNAs (49,050,000–76,690,000; T2T-CHM13 genome assembly) could not be mapped to GRCh38 coordinates because this sequence does not exist in GRCh38. The location of this repeat in GRCh38 was therefore estimated by checking where consecutive 10 kb bins around the centromere map in the T2T-CHM13 genome assembly; UCSC lift Genome Annotations; https://genome.ucsc.edu/cgi-bin/hgLiftOver. The start position of the first bin that maps after the repeat (in the T2T-CHM13 genome assembly) is considered to be the start of the repeat and the end position of the last bin that maps before the repeat as the end of the repeat. Note, this sequence in GRCh38 is scrambled; some parts map before and some parts map after this repeat in the T2T-CHM13 genome assembly.

Western blot

For western blotting of FKBP12, monoclonal RPE1 dCas9-Kin14VIb and its parental polyclonal population were transfected with 20 nM of siRNA Luciferase (CGUACGCGGAAUACUUCGAdTdT) siRNA FKBP12 (AAACUGGAAUGACAGGAAdTdT) using HyPerFect (Qiagen). 72 h following transfection, cells were lysed in Laemmli buffer for 10 min at 100°C. Protein concentration was determined using a Lowry assay. Proteins were separated on a 15% SDS-polyacrylamide (PAGE) by electrophoresis and transferred to a nitrocellulose membrane. The membrane was blocked with 5% milk in TBS-0.01% Tween-20 for 1 h, before being incubated with rabbit anti-FKBP12 antibodies (Abcam ab2918) at 4°C overnight. Horseradish peroxidase (HRP)-conjugated goat anti-rabbit secondary antibodies (Bioke, cat. no 7074) were then added for 2 h at room temperature. Chemiluminescence was detected using the WesternBright ECL system (Advansta K-12045-D20) and visualized using an Amersham Imager 600. The membrane was subsequently stripped by a 1-h incubation with PBS + 0.02% sodium azide and reprobed with mouse anti-Histone 3 antibodies (Abcam, ab1791) as a loading control. For the loading control, HRP-conjugated goat anti-mouse secondary antibodies (Biorad, 170-6516) were used.

Statistics

Where indicated, the mean and standard deviation (S.D.), or standard error of the mean (S.E.M.) are shown. Statistical significance was calculated with a Fisher's exact test, a nonparametric Student's *t*-test (Mann–Whitney test), nonparametric one-way ANOVA test with multiple comparison, or Kruskal–Wallis test with a Dann's multiple comparison test, using Prism 8 software.

Data availability

The single-cell whole-genome sequencing data for this study have been deposited in the European Nucleotide Archive (ENA) at EMBL-EBI under accession number PRJEB53741 (https://www.ebi.ac.uk/ena/browser/view/PRJEB53741).

Expanded View for this article is available online.

Author contributions

My Anh Truong: Conceptualization; formal analysis; investigation; visualization; methodology; writing – original draft; writing – review and editing. **Paula Cané-Gasull:** Formal analysis; validation; investigation; visualization; writing – review and editing. **Sippe G de Vries:** Investigation; methodology. **Wilco Nijenhuis:** Conceptualization; resources; methodology. **René Wardenaar:** Resources; formal analysis; methodology; writing – review and editing. **Lukas C Kapitein:** Conceptualization; resources; methodology. **Floris Foijer:** Resources; formal analysis; methodology; writing – review and editing. **Susanne M A Lens:** Conceptualization; formal analysis; supervision; funding acquisition; investigation; writing – original draft; project administration; writing – review and editing.

Disclosure and competing interests statement

The authors declare they have no conflict of interest.

References

Adikusuma F, Williams N, Grutzner F, Hughes J, Thomas P (2017) Targeted deletion of an entire chromosome using CRISPR/Cas9. *Mol Ther* 25: 1736–1738

Bakhoum SF, Thompson SL, Manning AL, Compton DA (2009) Genome stability is ensured by temporal control of kinetochore-microtubule dynamics. *Nat Cell Biol* 11: 27–35

Bakker B, Taudt A, Belderbos ME, Porubsky D, Spierings DCJ, de Jong TV, Halsema N, Kazemier HG, Hoekstra-Wakker K, Bradley A *et al* (2016) Single-cell sequencing reveals karyotype heterogeneity in murine and human malignancies. *Genome Biol* 17: 1–15

Ballister ER, Riegman M, Lampson MA (2014) Recruitment of Mad1 to metaphase kinetochores is sufficient to reactivate the mitotic checkpoint. *J Cell Biol* 204: 901–908

Ben-David U, Amon A (2020) Context is everything: aneuploidy in cancer. *Nat Rev Genet* 21: 44–62

Beuzer P, Quivy JP, Almouzni G (2014) Establishment of a replication fork barrier following induction of DNA binding in mammalian cells. *Cell Cycle* 13: 1607–1616

Bolhaqueiro ACF, Ponsioen B, Bakker B, Klaasen SJ, Kucukkose E, van Jaarsveld RH, Vivié J, Verlaan-Klink I, Hami N, Spierings DCJ *et al* (2019) Ongoing chromosomal instability and karyotype evolution in human colorectal cancer organoids. *Nature Genet* 51: 824–834

Bollen Y, Stelloo E, van Leenen P, van den Bos M, Ponsioen B, Lu B, van Roosmalen MJ, Bolhaqueiro ACF, Kimberley C, Mossner M *et al* (2021)

Reconstructing single-cell karyotype alterations in colorectal cancer identifies punctuated and gradual diversification patterns. *Nat Genet* 53: 1187–1195

van den Bos H, Spierings DCJ, Taudt AS, Bakker B, Porubský D, Falconer E, Novoa C, Halsema N, Kazemier HG, Hoekstra-Wakker K et al (2016) Single-cell whole genome sequencing reveals no evidence for common aneuploidy in normal and Alzheimer's disease neurons. *Genome Biol* 17: 116

Bosco N, Goldberg A, Zhao X, Mays JC, Cheng P, Johnson AF, Bianchi JJ, Toscani C, Tommaso E, Katsnelson L et al (2023) KaryoCreate: a CRISPR-based technology to study chromosome-specific aneuploidy by targeting human centromeres. *Cell* https://doi.org/10.1016/j.cell.2023

Chien MP, Werley CA, Farhi SL, Cohen AE (2015) Photostick: a method for selective isolation of target cells from culture. *Chem Sci* 6: 1701–1705

Dawe RK, Lowry EG, Gent JI, Stitzer MC, Swentowsky KW, Higgins DM, Ross-Ibarra J, Wallace JG, Kanizay LB, Alabady M et al (2018) A Kinesin-14 motor activates neocentromeres to promote meiotic drive in maize. *Cell* 173: 839–850

Doi G, Okada S, Yasukawa T, Sugiyama Y, Bala S, Miyazaki S, Kang D, Ito T (2021) Catalytically inactive Cas9 impairs DNA replication fork progression to induce focal genomic instability. *Nucleic Acids Res* 49: 954–968

Duijf PHG, Schultz N, Benezra R (2013) Cancer cells preferentially lose small chromosomes. *Int J Cancer* 132: 2316–2326

Dumont M, Gamba R, Gestraud P, Klaasen S, Worrall JT, Vries SGD, Boudreau V, Salinas-Luypaert C, Maddox PS, Lens SMA et al (2020) Human chromosome-specific aneuploidy is influenced by DNA-dependent centromeric features. *EMBO J* 39: e102924

Dunham MJ, Badrane H, Ferea T, Adams J, Brown PO, Rosenzweig F, Botstein D (2002) Characteristic genome rearrangements in experimental evolution of *Saccharomyces cerevisiae*. *Proc Natl Acad Sci U S A* 99: 16144–16149

Etemad B, Kuijt TEF, Kops GJPL (2015) Kinetochore-microtubule attachment is sufficient to satisfy the human spindle assembly checkpoint. *Nat Commun* 6: 8987

Fuller BG, Lampson MA, Foley EA, Rosasco-Nitcher S, Le KV, Tobelmann P, Brautigan DL, Stukenberg PT, Kapoor TM (2008) Midzone activation of aurora B in anaphase produces an intracellular phosphorylation gradient. *Nature* 453: 1132–1136

Gerstung M, Jolly C, Leshchiner I, Dentro SC, Gonzalez S, Rosebrock D, Mitchell TJ, Rubanova Y, Anur P, Yu K et al (2020) The evolutionary history of 2,658 cancers. *Nature* 578: 122–128

Gilbert LA, Larson MH, Morsut L, Liu Z, Brar GA, Torres SE, Stern-Ginossar N, Brandman O, Whitehead EH, Doudna JA et al (2013) CRISPR-mediated modular RNA-guided regulation of transcription in eukaryotes. *Cell* 154: 442–451

Godek KM, Kabeche L, Compton DA (2015) Regulation of kinetochore-microtubule attachments through homeostatic control during mitosis. *Nat Rev Mol Cell Biol* 16: 57–64

Gresham D, Desai MM, Tucker CM, Jenq HT, Pai DA, Ward A, DeSevo CG, Botstein D, Dunham MJ (2008) The repertoire and dynamics of evolutionary adaptations to controlled nutrient-limited environments in yeast. *PLoS Genet* 4: e1000303

Gut G, Herrmann MD, Pelkmans L (2018) Multiplexed protein maps link subcellular organization to cellular states. *Science* 361: eaar7042

Hindriksen S, Bramer AJ, Truong MA, Vromans MJM, Post JB, Verlaan-Klink I, Snippert HJ, Lens SMA, Hadders MA (2017) Baculoviral delivery of CRISPR/Cas9 facilitates efficient genome editing in human cells. *PLoS One* 12: e0179514

Hintzen DC, Soto M, Schubert M, Bakker B, Spierings DCJ, Szuhai K, Lansdorp PM, Kluin RJC, Foijer F, Medema RH et al (2022) The impact of monosomies, trisomies and segmental aneuploidies on chromosomal stability. *PLoS One* 17: e0268579

Howden SE, McColl B, Glaser A, Vadolas J, Petrou S, Little MH, Elefanty AG, Stanley EG (2016) A Cas9 variant for efficient generation of indel-free Knockin or gene-corrected human pluripotent stem cells. *Stem Cell Rep* 7: 508–517

Ippolito MR, Martis V, Martin S, Tijhuis AE, Hong C, Wardenaar R, Dumont M, Zerbib J, Spierings DCJ, Fachinetti D et al (2021) Gene copy-number changes and chromosomal instability induced by aneuploidy confer resistance to chemotherapy. *Dev Cell* 56: 2440–2454

Jacome A, Fernandez-Capetillo O (2011) Lac operator repeats generate a traceable fragile site in mammalian cells. *EMBO Rep* 12: 1032–1038

Janicki SM, Tsukamoto T, Salghetti SE, Tansey WP, Sachidanandam R, Prasanth KV, Ried T, Shav-Tal Y, Bertrand E, Singer RH et al (2004) From silencing to gene expression: real-time analysis in single cells. *Cell* 116: 683–698

Janssen A, Van Der Burg M, Szuhai K, Kops GJPL, Medema RH (2011) Chromosome segregation errors as a cause of DNA damage and structural chromosome aberrations. *Science* 333: 1895–1898

Jonsson E, Yamada M, Vale RD, Goshima G (2015) Clustering of a kinesin-14 motor enables processive retrograde microtubule-based transport in plants. *Nat Plants* 1: 1–7

Klaasen SJ, Truong MA, van Jaarsveld RH, Koprivec I, Štimac V, de Vries SG, Risteski P, Kodba S, Vukušić K, de Luca KL et al (2022) Nuclear chromosome locations dictate segregation error frequencies. *Nature* 607: 604–609

Knouse KA, Davoli T, Elledge SJ, Amon A (2017) Aneuploidy in cancer: seq-ing answers to old questions. *Annu Rev Cancer Biol* 1: 335–354

Krupina K, Goginashvili A, Cleveland DW (2021) Causes and consequences of micronuclei. *Curr Opin Cell Biol* 70: 91–99

Kuhn J, Dumont S (2017) Spindle assembly checkpoint satisfaction occurs via end-on but not lateral attachments under tension. *J Cell Biol* 216: 1533–1542

Leibowitz ML, Papathanasiou S, Doerfler PA, Blaine LJ, Sun L, Yao Y, Zhang CZ, Weiss MJ, Pellman D (2021) Chromothripsis as an on-target consequence of CRISPR–Cas9 genome editing. *Nat Genet* 53: 895–905

Liberles SD, Diver ST, Austin DJ, Schreiber SL (1997) Inducible gene expression and protein translocation using nontoxic ligands identified by a mammalian three-hybrid screen. *Proc Natl Acad Sci* 94: 7825–7830

Liu S, Kwon M, Mannino M, Yang N, Renda F, Khodjakov A, Pellman D (2018) Nuclear envelope assembly defects link mitotic errors to chromothripsis. *Nature* 561: 551–555

Lukow DA, Sausville EL, Suri P, Chunduri NK, Wieland A, Leu J, Smith JC, Girish V, Kumar AA, Kendall J et al (2021) Chromosomal instability accelerates the evolution of resistance to anti-cancer therapies. *Dev Cell* 56: 2427–2439

Ly P, Eskiocak U, Kim SB, Roig AI, Hight SK, Lulla DR, Zou YS, Batten K, Wright WE, Shay JW (2011) Characterization of aneuploid populations with trisomy 7 and 20 derived from diploid human colonic epithelial cells. *Neoplasia* 13: 348–357

Ly P, Teitz LS, Kim DH, Shoshani O, Skaletsky H, Fachinetti D, Page DC, Cleveland DW (2016) Selective Y centromere inactivation triggers chromosome shattering in micronuclei and repair by non-homologous end joining. *Nat Cell Biol* 19: 68–75

Ma H, Naseri A, Reyes-Gutierrez P, Wolfe SA, Zhang S, Pederson T (2015) Multicolor CRISPR labeling of chromosomal loci in human cells. *Proc Natl Acad Sci U S A* 112: 3002–3007

Ma H, Tu LC, Naseri A, Huisman M, Zhang S, Grunwald D, Pederson T (2016) Multiplexed labeling of genomic loci with dCas9 and engineered sgRNAs using CRISPRainbow. *Nat Biotechnol* 34: 528–530

Ma H, Tu LC, Naseri A, Chung YC, Grunwald D, Zhang S, Pederson T (2018) CRISPR-Sirius: RNA scaffolds for signal amplification in genome imaging. *Nat Methods* 15: 928–931

Maciejowski J, Li Y, Bosco N, Campbell PJ, De Lange T (2015) Chromothripsis and Kataegis induced by telomere crisis. *Cell* 163: 1641–1654

Maiato H, Afonso O, Matos I (2015) A chromosome separation checkpoint: a midzone Aurora B gradient mediates a chromosome separation checkpoint that regulates the anaphase-telophase transition. *Bioessays* 37: 257–266

Maiato H, Gomes AM, Sousa F, Barisic M (2017) Mechanisms of chromosome Congression during mitosis. *Biol* 6: 13–68

Musacchio A, Salmon ED (2007) (2007) the spindle-assembly checkpoint in space and time. *Nat Rev Mol Cell Biol* 85: 379–393

Nicholson JM, Macedo JC, Mattingly AJ, Wangsa D, Camps J, Lima V, Gomes AM, Dória S, Ried T, Logarinho E et al (2015) Chromosome mis-segregation and cytokinesis failure in trisomic human cells. *Elife* 4: e05068

Nijenhuis W, van Grinsven MMP, Kapitein LC (2020) An optimized toolbox for the optogenetic control of intracellular transport. *J Cell Biol* 219: e201907149

Nurk S, Koren S, Rhie A, Rautiainen M, Bzikadze AV, Mikheenko A, Vollger MR, Altemose N, Uralsky L, Gershman A et al (2022) The complete sequence of a human genome. *Science* 376: 44–53

Passerini V, Ozeri-Galai E, De Pagter MS, Donnelly N, Schmalbrock S, Kloosterman WP, Kerem B, Storchová Z (2016) The presence of extra chromosomes leads to genomic instability. *Nat Commun* 7: 1–12

Rancati G, Pavelka N, Fleharty B, Noll A, Trimble R, Walton K, Perera A, Staehling-Hampton K, Seidel CW, Li R (2008) Aneuploidy underlies rapid adaptive evolution of yeast cells deprived of a conserved cytokinesis motor. *Cell* 135: 879–893

Ravichandran MC, Fink S, Clarke MN, Hofer FC, Campbell CS (2018) Genetic interactions between specific chromosome copy number alterations dictate complex aneuploidy patterns. *Genes Dev* 32: 1485–1498

Rivera VM, Clackson T, Natesan S, Pollock R, Amara JF, Keenan T, Magari SR, Phillips T, Courage NL, Franklin Cerasoli JR et al (1996) A humanized system for pharmacologic control of gene expression. *Nat Med* 2: 1028–1032

Sack LM, Davoli T, Li MZ, Li Y, Xu Q, Naxerova K, Wooten EC, Bernardi RJ, Martin TD, Chen T et al. (2018) Profound tissue specificity in proliferation control underlies cancer drivers and aneuploidy patterns. *Cell* 173: 499–514

Sakaue-Sawano A, Yo M, Komatsu N, Hiratsuka T, Kogure T, Hoshida T, Goshima N, Matsuda M, Miyoshi H, Miyawaki A (2017) Genetically encoded tools for optical dissection of the mammalian cell cycle. *Mol Cell* 68: 626–640

Santaguida S, Richardson A, Iyer DR, M'Saad O, Zasadil L, Knouse KA, Wong YL, Rhind N, Desai A, Amon A (2017) Chromosome mis-segregation generates cell-cycle-arrested cells with complex karyotypes that are eliminated by the immune system. *Dev Cell* 41: 638–651

Sareen D, McMillan E, Ebert AD, Shelley BC, Johnson JA, Meisner LF, Svendsen CN (2009) Chromosome 7 and 19 trisomy in cultured human neural progenitor cells. *PLoS One* 4: e7630

Sedelnikova OA, Rogakou EP, Panyuntin IG, Bonner WM (2002) Quantitative detection of 125IdU-induced DNA double-Strand breaks with γ-H2AX antibody. *Radiat Res* 158: 482–492

Sen O, Harrison JU, Burroughs NJ, McAinsh AD (2021) Kinetochore life histories reveal an Aurora-B-dependent error correction mechanism in anaphase. *Dev Cell* 56: 3082–3099

Shen Z, Collatos AR, Bibeau JP, Furt F, Vidali L (2012) Phylogenetic analysis of the kinesin superfamily from Physcomitrella. *Front Plant Sci* 3: 230

Soto M, Raaijmakers JA, Bakker B, Spierings DCJ, Lansdorp PM, Foijer F, Medema RH (2017) p53 prohibits propagation of chromosome segregation errors that produce structural aneuploidies. *Cell Rep* 19: 2423–2431

Su XA, Ma D, Parsons JV, Replogle JM, Amatruda JF, Whittaker CA, Stegmaier K, Amon A (2021) RAD21 is a driver of chromosome 8 gain in Ewing sarcoma to mitigate replication stress. *Genes Dev* 35: 556–572

Taylor AM, Shih J, Ha G, Gao GF, Zhang X, Berger AC, Schumacher SE, Wang C, Hu H, Liu J et al (2018) Genomic and functional approaches to understanding cancer aneuploidy. *Cancer Cell* 33: 676–689

Thomas R, Marks DH, Chin Y, Benezra R (2018) Whole chromosome loss and associated breakage–fusion–bridge cycles transform mouse tetraploid cells. *EMBO J* 37: 201–218

Tovini L, McClelland SE (2019) Impaired CENP-E function renders large chromosomes more vulnerable to Congression failure. *Biomolecules* 9: 44

Tovini L, Johnson SC, Guscott MA, Andersen AM, Spierings DCJ, Wardenaar R, Foijer F, McClelland SE (2023) Targeted assembly of ectopic kinetochores to induce chromosome-specific segmental aneuploidies. *EMBO J* 42: e111587

Umbreit NT, Zhang CZ, Lynch LD, Blaine LJ, Cheng AM, Tourdot R, Sun L, Almubarak HF, Judge K, Mitchell TJ et al (2020) Mechanisms generating cancer genome complexity from a single cell division error. *Science* 368: eaba0712

Upender MB, Habermann JK, McShane LM, Korn EL, Barrett JC, Difilippantonio MJ, Ried T (2004) Chromosome transfer induced aneuploidy results in complex dysregulation of the cellular transcriptome in immortalized and cancer cells. *Cancer Res* 64: 6941–6949

Viganó C, von Schubert C, Ahrné E, Schmidt A, Lorber T, Bubendorf L, De Vetter JRF, Zaman GJR, Storchova Z, Nigg EA (2018) Quantitative proteomic and phosphoproteomic comparison of human colon cancer DLD-1 cells differing in ploidy and chromosome stability. *Mol Biol Cell* 29: 1031–1047

Whinn KS, Kaur G, Lewis JS, Schauer GD, Mueller SH, Jergic S, Maynard H, Gan ZY, Naganbabu M, Bruchez MP et al (2019) Nuclease dead Cas9 is a programmable roadblock for DNA replication. *Sci Rep* 91: 1–9

Worrall JT, Tamura N, Mazzagatti A, Shaikh N, van Lingen T, Bakker B, Spierings DCJ, Vladimirou E, Foijer F, McClelland SE (2018) Non-random mis-segregation of human chromosomes. *Cell Rep* 23: 3366–3380

Yamada M, Tanaka-Takiguchi Y, Hayashi M, Nishina M, Goshima G (2017) Multiple kinesin-14 family members drive microtubule minus end-directed transport in plant cells. *J Cell Biol* 216: 1705–1714

Yu HG, Hiatt EN, Chan A, Sweeney M, Dawe RK (1997) Neocentromere-mediated chromosome movement in maize. *J Cell Biol* 139: 831–840

Zack TI, Schumacher SE, Carter SL, Cherniack AD, Saksena G, Tabak B, Lawrence MS, Zhang CZ, Wala J, Mermel CH et al (2013) Pan-cancer patterns of somatic copy number alteration. *Nat Genet* 45: 1134–1140

Zhang CZ, Spektor A, Cornils H, Francis JM, Jackson EK, Liu S, Meyerson M, Pellman D (2015) Chromothripsis from DNA damage in micronuclei. *Nature* 522: 179–184

Zuo E, Huo X, Yao X, Hu X, Sun Y, Yin J, He B, Wang X, Shi L, Ping J et al (2017) CRISPR/Cas9-mediated targeted chromosome elimination. *Genome Biol* 18: 224–241
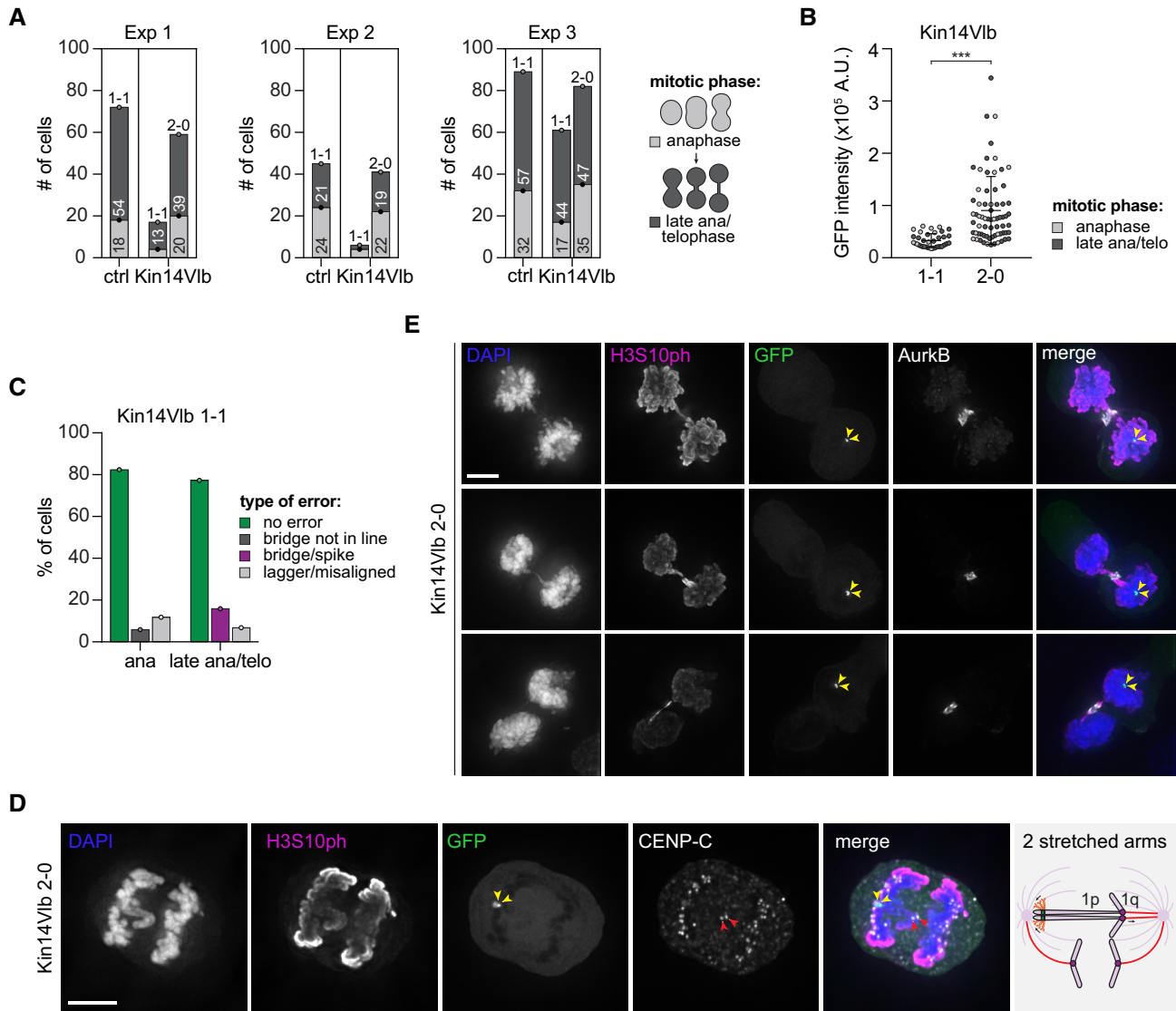
Expanded View Figures

Figure EV1 (related to Fig 3). Segregation of the Kin14VIb-bound TetO chromosome during anaphase and telophase.

A Number of analyzed cells displaying a 1-1 or 2-0 distribution of the TetO locus in the three biological replicates shown in Fig 3. Schemes on the right show how the anaphase and late anaphase/telophase cells were classified.

B Quantification of cytoplasmic GFP intensity in TetR-GFP-Kin14VIb-expressing cells that display either a 1-1 or a 2-0 distribution of the TetO locus from replicate 3. Light- and dark-colored dots represent individual cells in anaphase and in late anaphase/telophase, respectively.

C Frequency of the various types of segregation errors observed in anaphase and late anaphase/telophase of TetR-GFP-Kin14VIb expressing cells, displaying a 1-1 distribution of the TetO locus. Because of the low cell numbers of this category in experiments 1 and 2 (see A), only cells from experiment 3 were scored.

D Representative IF images of a U-2 OS TetO cell expressing TetR-GFP-Kin14VIb displaying a 2-0 distribution of the TetO locus and with two stretched arms in line with the TetO locus near the spindle pole. For clarity, the maximum intensity projection of a subset of z stacks (6/50) is shown. Scale bar = 5 μm. Scheme illustrating the anaphase orientation of the TetO sister chromatids is shown on the right. While Kin14VIb pulls the p-arm telomeres of the TetO chromosome toward one pole, its sister KTs are syntelically attached to MTs coming from the opposite spindle pole, thereby causing the two sister arms to stretch across the two spindle poles. Yellow arrowheads indicate the TetO locus, and white arrowheads point at the lagging KTs on the stretched arms.

E IF for Aurora B, GFP, H3S10ph of U-2 OS TetO cells in anaphase and telophase expressing rTetR-GFP-Kin14VIb and displaying a 2-0 distribution of the TetO locus (yellow arrowheads). The stretched chromatid arm (visible with H3S10ph) gets trapped into the cytokinetic furrow and midbody, highlighted by the respective midzone and midbody localization of Aurora B. Scale bar = 5 μm. DNA is visualized with DAPI.

Data information: (A): Exp 1, n = 17 cells for Kin14VIb 1-1; exp 2, n = 6 cells for Kin14VIb 1-1. (B): Mean and S.D. are shown. Each dot represents one individual cell. N = 38 cells for category "1-1", and n = 69 cells for category "2-0". ***P< 0.001, Mann–Whitney test.

Figure EV2 (related to Fig 4).   Single nuclei karyotypes of U-2 OS TetO cells.

A   Scheme of the experimental setup for the single-cell whole-genome sequencing of U-2 OS TetO cells shown in Fig 4C.

B, C   Genome-wide copy number heatmap of the nontransduced U-2 OS TetO cells (nontransduced) (B), and heatmaps showing the copy number alterations relative to the median copy karyotype in nontransduced cells, or cells transduced with rTetR-GFP or rTetR-GFP-Kin14VIb (C). Individual cells are in rows and genome positions in columns. Chromosome boundaries are indicated with black lines and colors are corresponding to the most likely copy number state per bin as determined by AneuFinder. The median copy number was determined for each bin (median across libraries) of the nontransduced libraries to produce a median (consensus) karyotype (colored line below heatmap in (B)). The latter was used as reference to generate heatmaps showing the copy number alterations relative to the U-2 OS TetO median karyotype for nontransduced (upper), rTetR-GFP-transduced (middle), or rTetR-GFP-Kin14VIb-transduced (lower) U-2 OS TetO cells in (C).
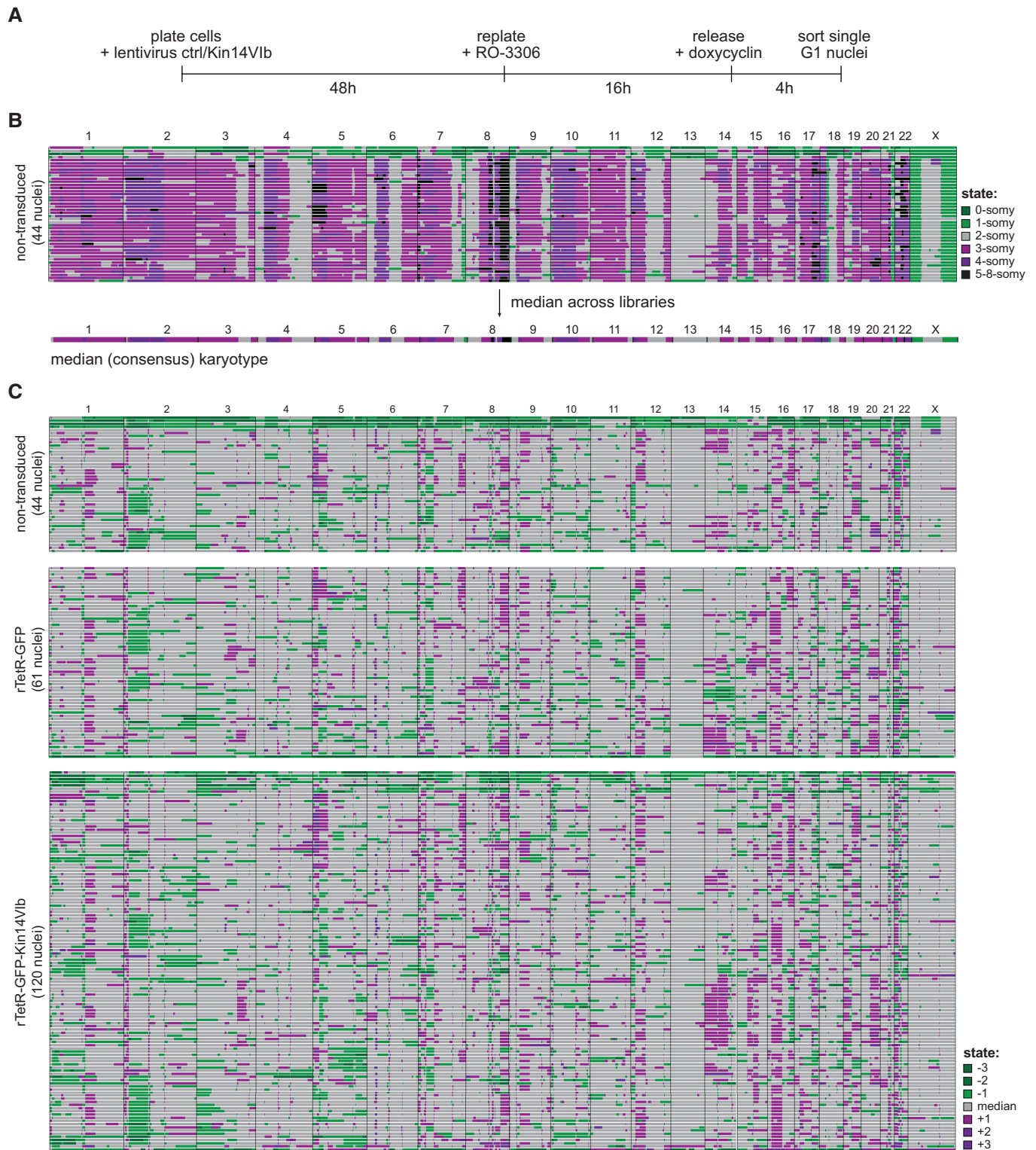
A

plate cells
+ lentivirus ctrl/Kin14VIb

replate
+ RO-3306

release
+ doxycyclin

sort single
G1 nuclei

48h   16h   4h

B

median across libraries

median (consensus) karyotype

state:
- 0-somy
- 1-somy
- 2-somy
- 3-somy
- 4-somy
- 5-8-somy

C

non-transduced
(44 nuclei)

rTetR-GFP
(61 nuclei)

rTetR-GFP-Kin14VIb
(120 nuclei)

state:
- -3
- -2
- -1
- median
- +1
- +2
- +3

Figure EV2 (related to Fig 4).

Figure EV3 (related to Fig 1). Tethering Kin14Vlb to the TetO repeat on Chr1p36 in U-2 OS cells increases micronuclei formation.

A   Percentage of U-2 OS cell divisions that gave rise to a micronucleus (MN) in at least one of the daughter cells. MN originating either from a chromatin bridge/spike, or a misaligned chromosome were scored from the live-cell imaging experiment shown in Fig 1. Ctrl or Kin14Vlb-expressing cells displaying either 1-1, or a 2-0 distribution of the TetO locus were scored. The scheme on the right illustrates a chromatin bridge/spike, and a misaligned chromosome in anaphase/telophase.

B   Representative stills from live-cell microscopy experiment showing GFP- or GFP+ MN from different origins, of cells displaying a 1-1 (top), or a 2-0 (bottom) TetO locus distribution in anaphase. Scale bar = 5 μm. Time = h:min. Schemes below the images illustrate TetO locus segregation during anaphase, and its subsequent fate (MN formation or incorporation into main nucleus) in the daughters. Yellow arrowheads indicate bridge/spike, white arrowheads point at the TetO locus, and asterisks indicate MN.

Data information: *N* = 55 cells for ctrl 1-1, *n* = 27 cells for Kin14Vlb 1-1 and *n* = 28 cells for Kin14Vlb 2-0.
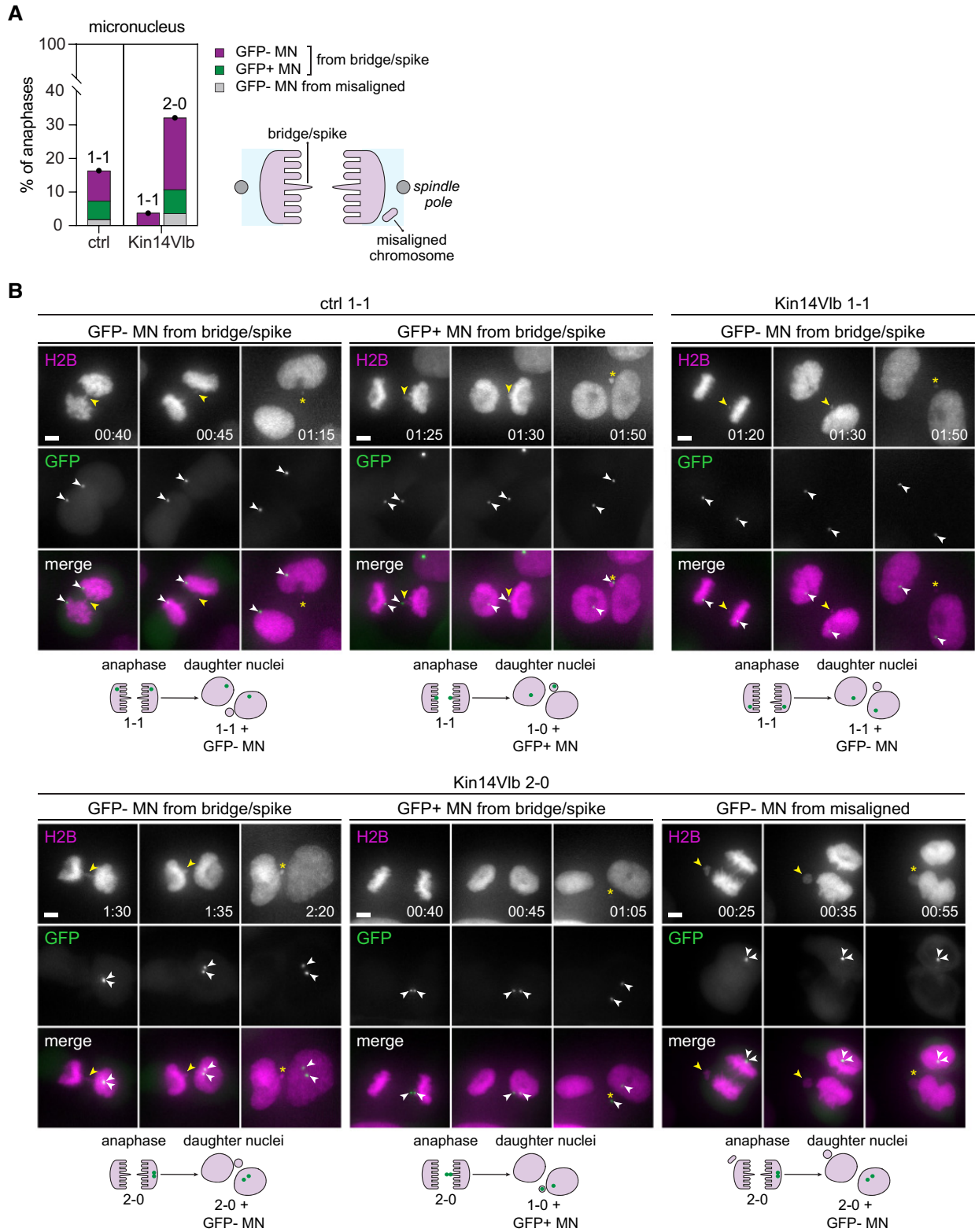
Figure EV3 (related to Fig 1).

Figure EV4 (related to Fig 8).   Breakpoint analysis of chromosome 9.

A   Scheme of the experimental setup for the single-cell whole-genome sequencing of RPE1 dCas9-Kin14VIb cells shown in Fig 8.

B   Original positions of the breakpoints on Chr9 as determined by AneuFinder. Some cells lost one or two q arms (green and dark green dots, respectively), or gained one or two q arms (purple and dark purple dots, respectively). The brown striped rectangle depicts the estimated location (in Mb) of the repetitive region targeted by Chr9-cen sgRNAs in the CRCh38 genome build (see methods). The black dot indicates the position of the centromere. Light gray rectangles at the bottom indicate the positions of the bins. The breakpoints (colored dots) were refined using the information of single reads. The breakpoint positions therefore do not match with the start positions of the bins, especially within the repetitive region. The yellow rectangle selects one single cell, for which the breakpoint estimation by Aneufinder was incorrect. The profile plot and breakpoint estimation by Aneufinder for this cell is shown on the right. Two pericentromeric bins with aberrant reads are indicated as red dots.

C   Picture showing the implementation of the shifting breakpoint approach (see materials and methods). The top figure shows the read counts of the bins (black dots), while the bottom figure shows the RSS values (purple dots) for different breakpoints. The black solid line with an arrow shows the breakpoint that is tested, and the small black arrows attached to each point indicate the difference between the read count of the bin and the mean of the state it is expected to belong to. The bin that comes before the tested breakpoints is expected to be 2-somy, and the bin after would be 1-somy.

D   Results from residual sum of squares analysis (shifting breakpoint analysis). The green and purple colored dots are stacked because breakpoints match with the start positions of the bins. Two bins that have an overlap with the pericentromeric repeat were not included in this analysis (aberrant read count; dark gray dots; see also (E): for bin 0 and 1, read count is higher than expected). The yellow rectangle selects the same single cell as in C, with its profile plot and shifted breakpoint shown on the right.

E   Boxplot of noninteger copy numbers for cells with 9q 1-somy or 0-somy (green), 9q euploidy (gray), or 9q 3-somy or 4-somy (purple) (from +rapalog cells, Fig 8A). Central black lines represent the median and boxes cover the interquartile range (IQR = 25th-75th percentile). Whiskers below or on top of the boxes have a maximum length of $1.5 \times$ IQR and, respectively, indicate the lowest or highest data point within this range. Data points falling outside the whisker range are considered outliers and shown as individual dots. If there is no data point within the whisker range, or if the highest or lowest data point coincides with the end or the beginning of the IQR, then no whisker is shown. Bin number is relative to the centromere bin (Bin 0). Gray rectangles at the top indicate the positions and sizes of the bins. Numbers at the top indicate start and end positions of the pericentromeric repeat bins (dark gray; in Mb). The gray horizontal line marks the expected copy number for diploidy (copy number = 2). The bottom part of the figure indicates the significance of the difference in copy number between cells that lost or gained one or two q arm copies (Wilcoxon rank-sum test; (NS) not significant, ***$P < 0.001$).
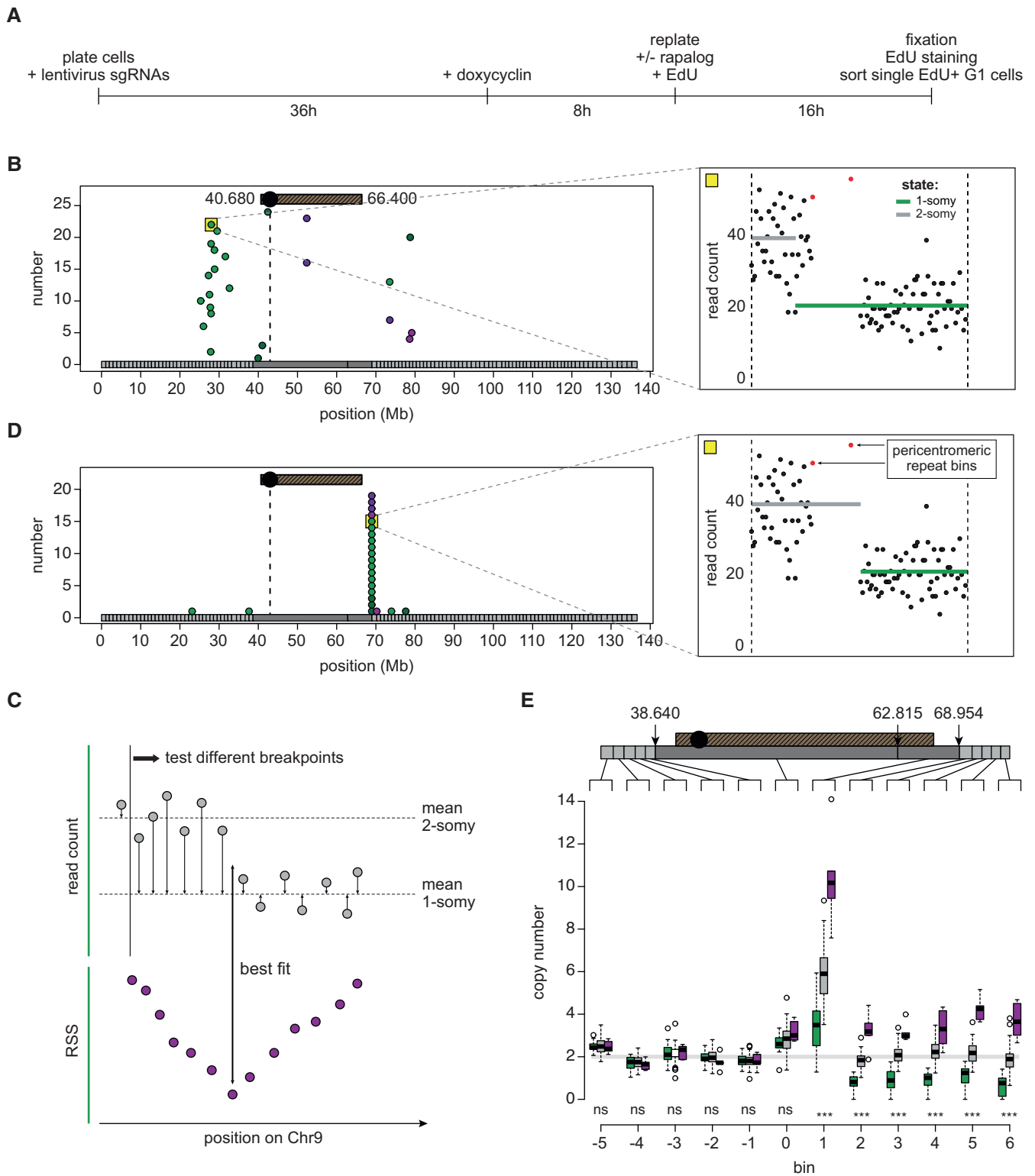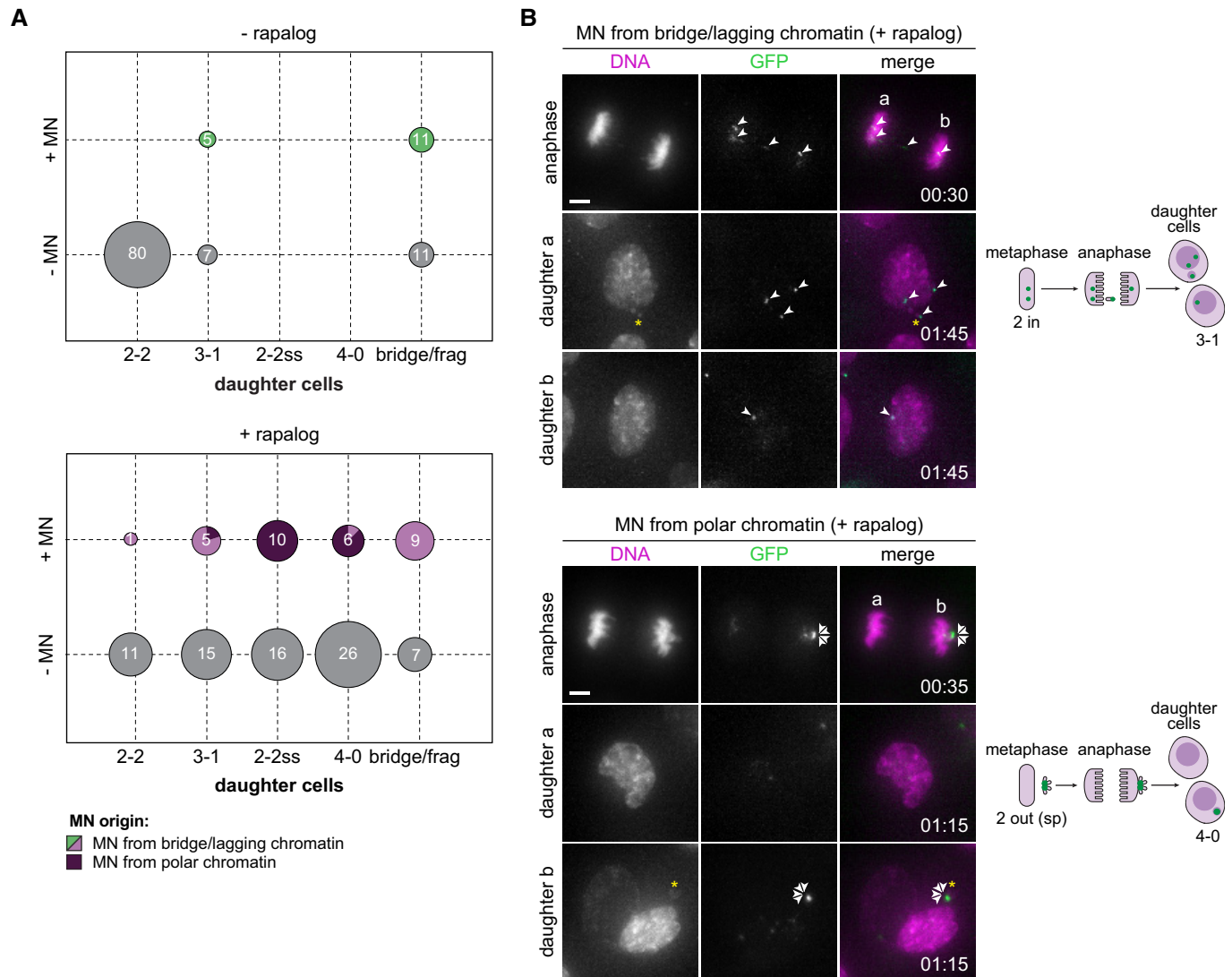
Figure EV4 (related to Fig 8).

Figure EV5 (related to Fig 6). Coupling Kin14VIb to Chr9-cen induces micronuclei formation in a fraction of the daughter cells.

A Plots showing the relationship between the indicated daughter cell distribution of Chr9-cen loci (x-axis), and daughter cells with a micronucleus (+MN) or without a MN (−MN, y-axis). Circle size reflects relative daughter cell numbers. The actual cell numbers per condition are indicated in the circles. Ss = same sisters. The origin of the MN (either bridge or lagging chromatin, or polar chromatin) is color coded as indicated.

B Representative stills of a rapalog-treated cell with a lagging locus in anaphase and leading to a 3-1 daughter cell distribution, with daughter cell (a) harboring a GFP+ MN (top panel), or of a rapalog-treated cell with a 4-0 segregation of the loci during anaphase, and eventually forming a GFP+ MN in daughter cell (b) (bottom panel). Schemes illustrating metaphase orientation, anaphase segregation and daughter cell distribution of the Chr9-cen loci are shown on the right. Letters in anaphase stills indicate the corresponding daughter cells in the images below. Stars and arrowheads indicate MN and Chr9-cen loci, respectively. Time = h:min. Scale bar = 5 μm. SiR-DNA was used to visualize the DNA, GFP depicts Chr9-cen loci.

Data information: Cells were derived from three independent live-cell imaging experiments, including the two shown in Fig 6. N = 57 cells (− rapalog), n = 53 cells (+ rapalog). (B) For optimal visibility of the Chr9-cen foci and the MN, brightness and contrast for these channels were linearly adjusted for individual cells.

A kinesin-based approach for inducing chromosome-specific mis-segregation in human cells

My Anh Truong[1,2,*], Paula Cané-Gasull[1,2,*], Sippe G. de Vries[1,2], Wilco Nijenhuis[3,4], René Wardenaar[5], Lukas C. Kapitein[3,4], Floris Foijer[5], Susanne M.A. Lens[1,2]

[1]Oncode Institute and [2]Center for Molecular Medicine, University Medical Center Utrecht, 3584 CG Utrecht, the Netherlands

[3]Cell Biology, Neurobiology and Biophysics, Department of Biology, Faculty of Science, Utrecht University, 3584 CH Utrecht, the Netherlands

[4]Centre for Living Technologies, Alliance TU/e, WUR, UU, UMC Utrecht, Princetonlaan 6, 3584 CB Utrecht, the Netherlands

[5]European Research Institute for the Biology of Ageing (ERIBA), University of Groningen, University Medical Center Groningen, 9713 AV Groningen, the Netherlands

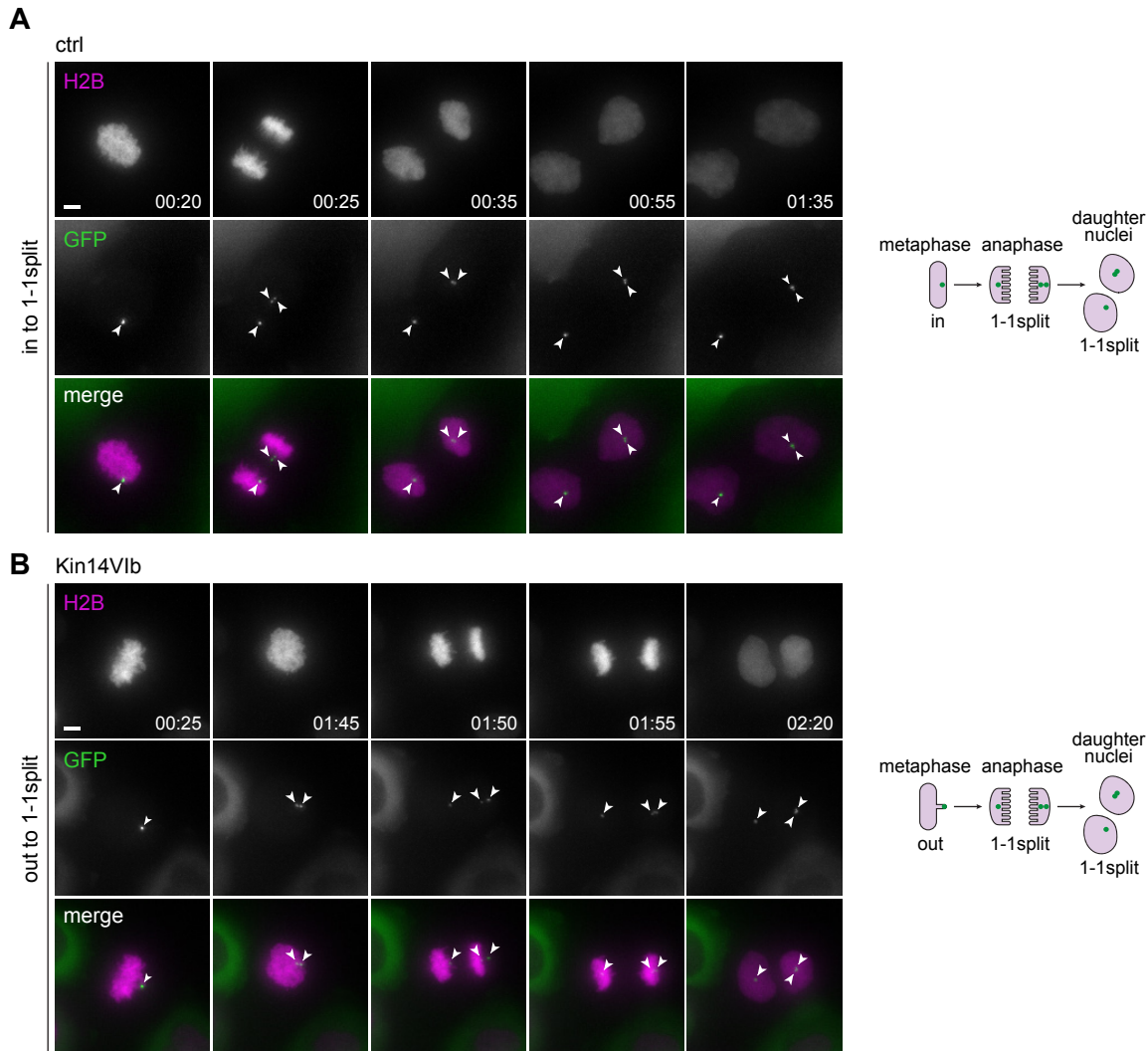*These authors contributed equally

Correspondence: S.M.A. Lens, PhD, Universiteitsweg 100, 3584 CG Utrecht, the Netherlands

Appendix
Table of content
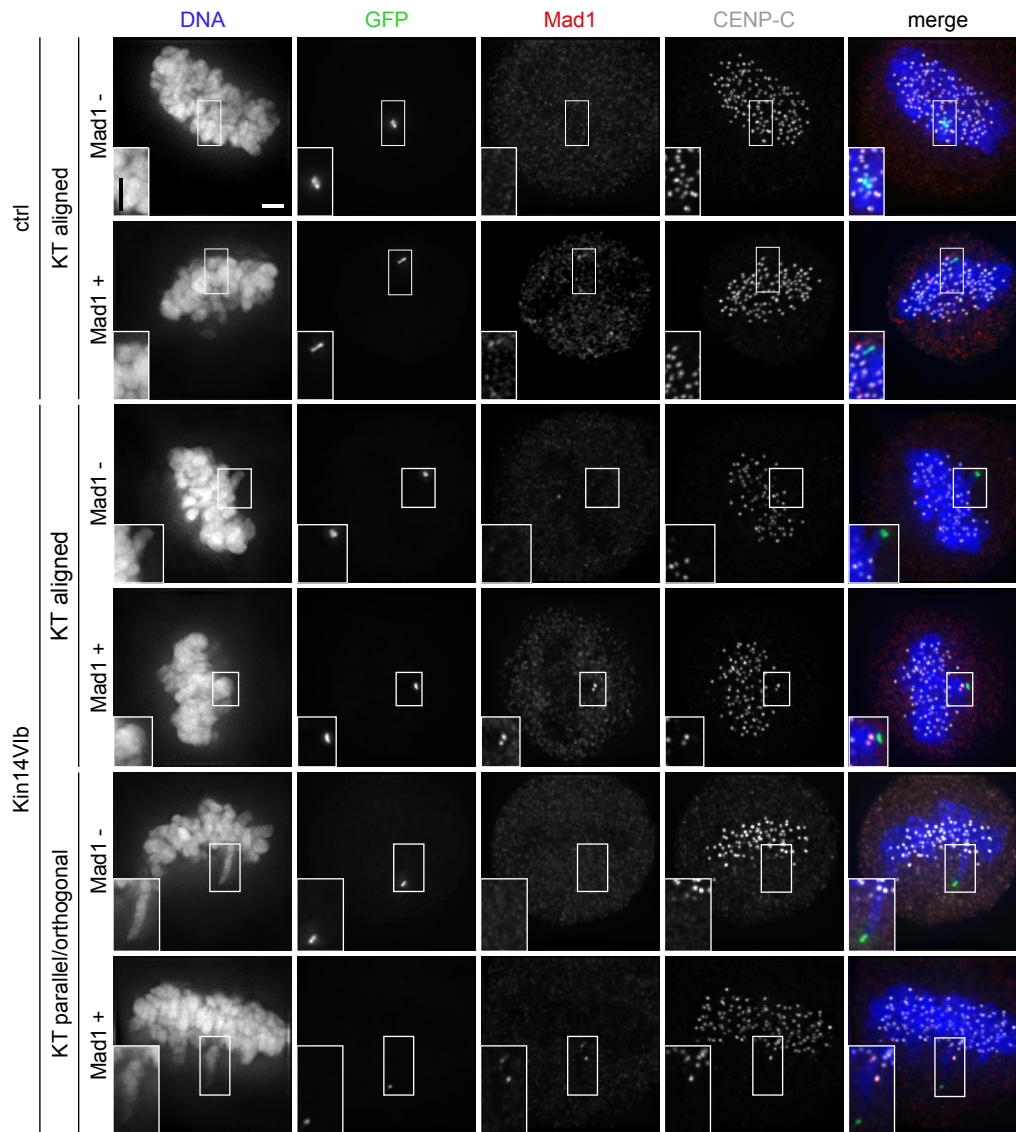
Appendix Figure S1

A

B

Appendix Figure S1: Examples of U-2 OS TetO cells displaying a 1-1split TetO locus distribution

A, B. Still images from the live microscopy experiment shown in Fig 1. Cells expressing either rTetR-GFP (ctrl, A) or rTetR-GFP-Kin14VIb (Kin14VIb, B), displaying a 1-1split distribution of the TetO locus (arrowheads). Schemes illustrating the metaphase localization, anaphase segregation, and daughter cell distribution of the TetO locus in each case are shown on the right. Scale bar = 5 μm. Time = h:min.

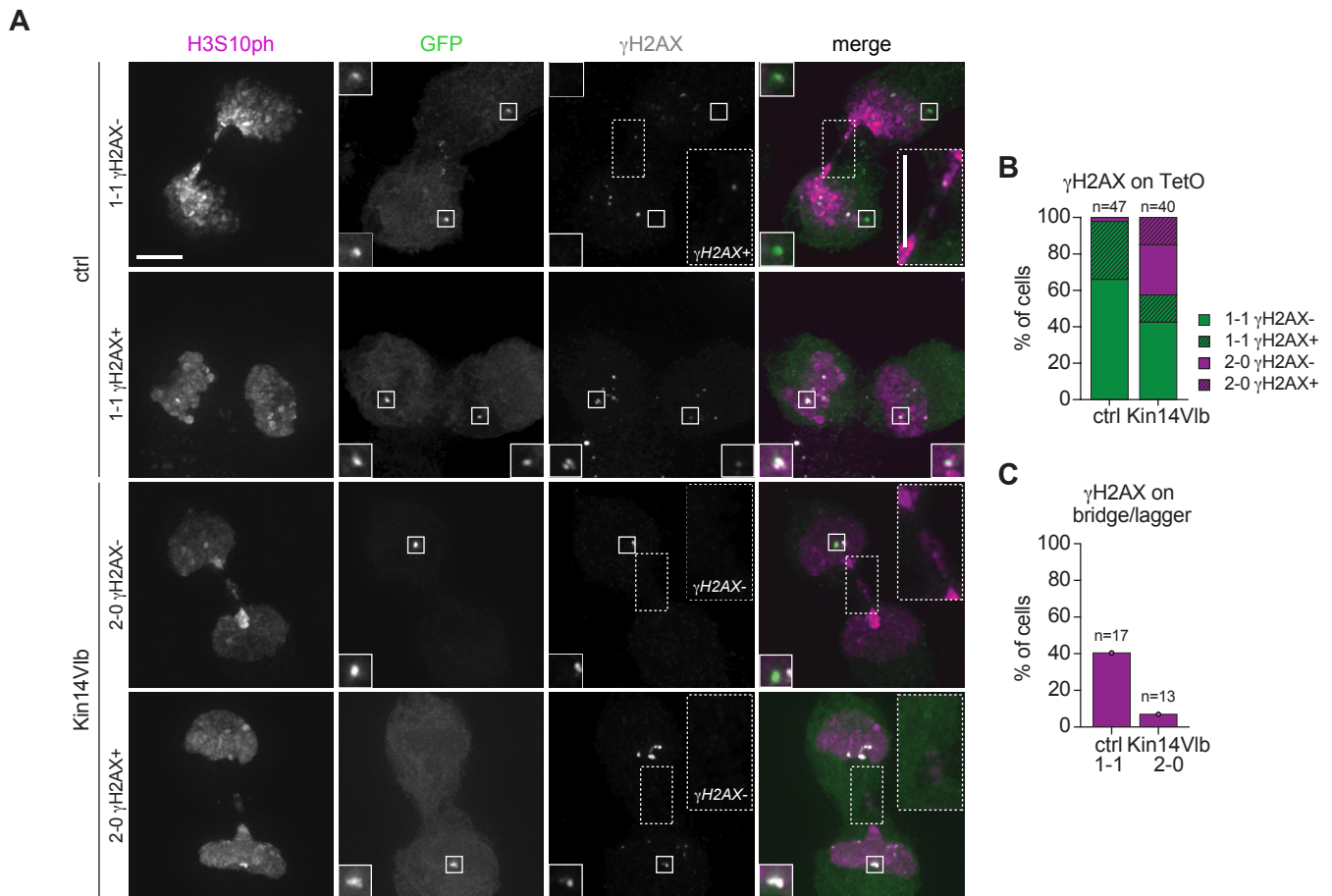**Appendix Figure S2**

A

Appendix Figure S2: Mad1 kinetochore localization in U-2 OS TetO cells

IF for GFP, Mad1 and CENP-C of U-2 OS-TetO cells in metaphase expressing rTetR-GFP (ctrl) or rTetR-GFP-Kin14VIb (Kin14VIb). Representative images of the different orientations of the TetO chromosome or locus and the sister KTs are shown. Magnifications of the white boxed indicating the TetO chromosome are shown at the corner of the images. For clarity, the maximum intensity projection of a subset of z-stacks in which the TetO locus is in focus (9-15/50) is shown. Scale bars = 2 µm. For optimal visibility of CENP-C, the brightness and contrast for this channel were linearly adjusted for individual cells.
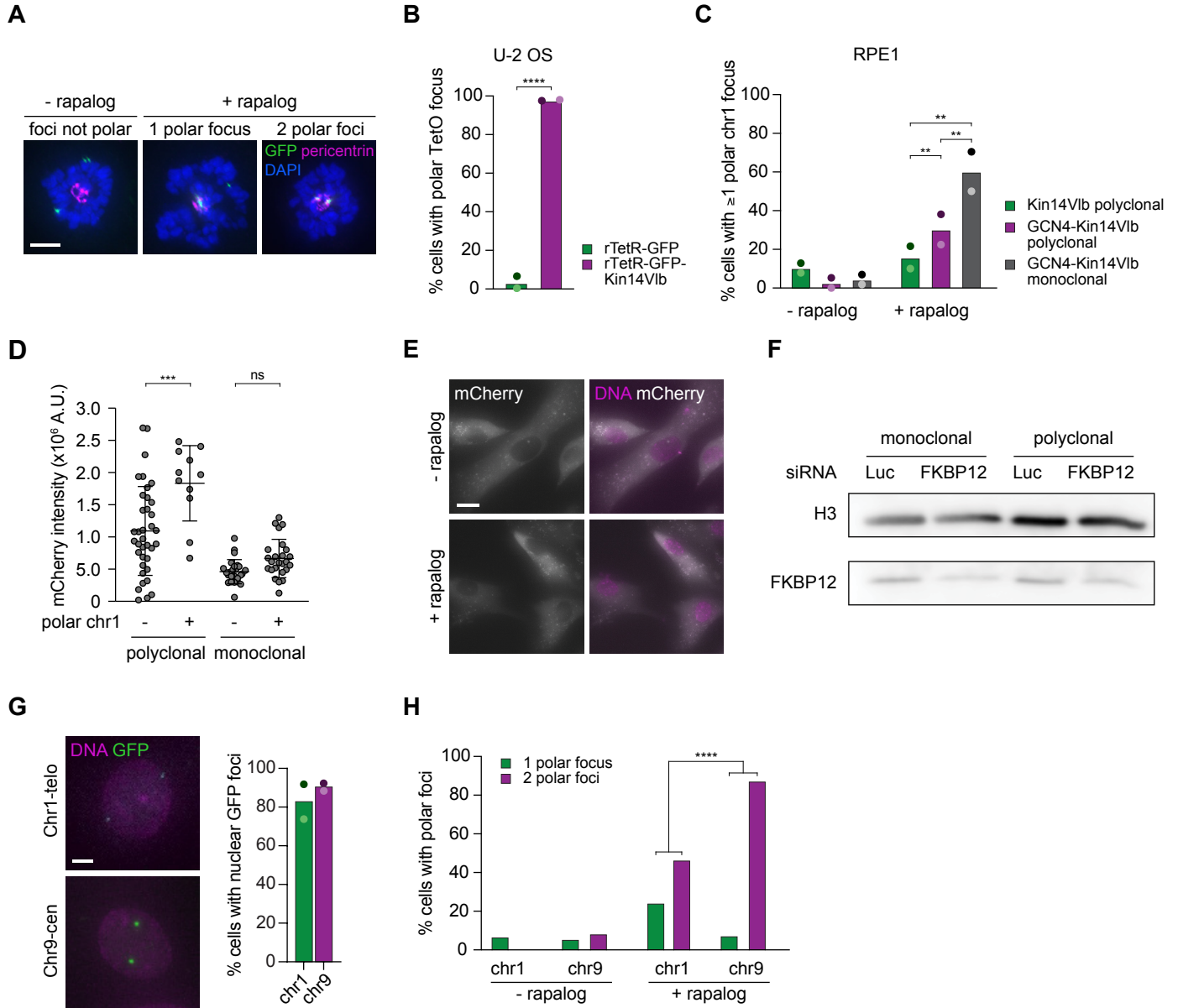
Appendix Figure S3

A

Appendix Figure S3. γH2AX is not detected on the TetO locus nor on the H3S10ph+ bridges in U-2 OS TetO cells expressing rTetR-GFP-Kin14VIb

A. Representative IF images of U-2 OS TetO cells in anaphase/telophase expressing rTetR-GFP (ctrl) or rTetR-GFP-Kin14VIb (Kin14VIb) and stained with the indicated antibodies. γH2AX was used as a marker for DNA damage. Magnifications of the white boxed regions are shown in the corners of the images. Solid lined boxes represent the GFP (TetO) foci, the dotted lined boxes chromatin bridges. Scale bars = 5 μm.

B. Quantification of γH2AX co-localization with the segregating TetO locus in U-2 OS cells expressing rTetR-GFP or rTetR-GFP-Kin14VIb.

C. Frequency of cells with γH2AX on chromatin bridges (incl. stretched arms) or lagging chromosomes during anaphase/telophase. N = number of cells with bridge/laggers.

Appendix Figure S4

A

B U-2 OS

C RPE1

D

E

F

G

H

Appendix Figure S4: Harnessing dCas9 to target Kin14Vlb to repetitive chromosomal loci in RPE1 cells

A. Representative IF images of STLC-treated mitotic RPE1 dCas9-Kin14Vlb cells displaying either 0, 1, or 2 polar Chr1-telo foci. Cells were transduced with lentivirus containing sgRNAs for 48 hours, followed by an overnight incubation with STLC and 1 *μ*g/ml doxycyclin to prevent centrosome separation and to induce FRB-mCherry-GCN4-Kin14Vlb expression, respectively. Rapalog was added 4 h prior to fixation. Scale bar = 5*μ*m.

B. Quantification of mitotic monopolar U-2 OS cells with a polar TetO focus. n ≥ 32 per condition, per experiment.

4

Appendix Figure S4: Harnessing dCas9 to target Kin14VIb to repetitive chromosomal loci in RPE1 cells

C. Quantification of mitotic monopolar RPE1 cells expressing dCas9-GFP-3xFKBP and FRB-mCherry-Kin14VIb dimers (polyclonal) or FRB-mCherry-GCN4-Kin14VIb tetramers (polyclonal or monoclonal), which display at least 1 polar Chr1-telo focus. n ≥ 31 per condition, per experiment.

D. Quantification of cytoplasmic mCherry fluorescence intensity levels in polyclonal and mono-clonal RPE1 dCas9-Kin14VIb cells expressing FRB-mCherry-GCN4-Kin14VIb, and displaying either 0, or at least 1 polar Chr1-telo foci as shown in A and C.

E. Representative images of RPE1 dCas9-Kin14VIb cells from the experiments in Fig 5A, showing FRB-mCherry-GCN4-Kin14VIb outside the nucleus in interphase cells. Scale bar = 20 μm.

F. Western blot of FKBP12 protein in polyclonal and monoclonal RPE1 dCas9-Kin14VIb cells (expressing GCN4-Kin14VIb). Cells were transfected with siRNA Luciferase (Luc) or siRNA FKBP 72 hours before lysis.

G. Representative images of interphase RPE1 dCas9-Kin14VIb cells transduced with Chr1-telo (top), or Chr9-cen sgRNA (bottom) and quantification of lentiviral transduction efficiency for Chr1-telo and Chr9-cen sgRNAs, indicated by the fraction of cells displaying focal localization of dCas9 (= GFP). Scale bar = 5 μm. Interphase cells from the experiments shown in Figs 5D and E and 6B and C were analysed.

H. Quantification of mitotic monopolar RPE1 dCas9-Kin14VIb cells that are transduced with either Chr1-telo or Chr9-cen sgRNAs and displaying 1 or 2 polar loci in the presence or absence of rapalog. Percentages from a single experiment are shown. N ≥ 35 per condition.

Data information: (B, C, G, H): Bars represent the mean of 2 independent experiments, while dark- and light-colored dots represent the individual values of each experiment. **** $P<0.0001$; ** $P< 0.01$; * $P< 0.05$, Fisher's exact test. (D): Each dot represents an individual cell. *** $p<0.001$; ns not significant ($p=0.4787$), one-way anova test with multiple comparisons.